

Safe and Non-Conservative Contingency Planning for Autonomous Vehicles via Online Learning-Based Reachable Set Barriers

Rui Yang, Lei Zheng, Shuzhi Sam Ge, *Fellow, IEEE*, and Jun Ma, *Senior Member, IEEE*

Abstract—Autonomous vehicles must navigate dynamically uncertain environments while balancing the safety and driving efficiency. This challenge is exacerbated by the unpredictable nature of surrounding human-driven vehicles (HVs) and perception inaccuracies, which require planners to adapt to evolving uncertainties while maintaining safe trajectories. Overly conservative planners degrade driving efficiency, while deterministic approaches may encounter serious issues and risks of failure when faced with sudden and unexpected maneuvers. To address these issues, we propose a real-time contingency trajectory optimization framework in this paper. By employing event-triggered online learning of HV control-intent sets, our method dynamically quantifies multi-modal HV uncertainties and refines the forward reachable set (FRS) incrementally. Crucially, we enforce invariant safety through FRS-based barrier constraints that ensure safety without reliance on accurate trajectory prediction of HVs. These constraints are embedded in contingency trajectory optimization and solved efficiently through consensus alternative direction method of multipliers (ADMM). The system continuously adapts to the uncertainties in HV behaviors, preserving feasibility and safety without resorting to excessive conservatism. High-fidelity simulations on highway and urban scenarios, as well as a series of real-world experiments demonstrate significant improvements in driving efficiency and passenger comfort while maintaining safety under uncertainty. The project page is available at <https://pathetiue.github.io/frscp.github.io/>.

Index Terms—Autonomous vehicles, trajectory optimization, reachability analysis, contingency planning.

I. INTRODUCTION

ENSURING the safety of autonomous vehicles in dynamic, uncertain environments is paramount. This requires strict safety guarantees without unnecessarily compromising driving efficiency [1], [2]. A core challenge lies in accurately modeling and adapting to the uncertain, time-varying behaviors of surrounding human-driven vehicles (HVs), compounded by perception inaccuracies [3], [4]. Unanticipated contingency events, such as abrupt lane changes or sudden acceleration/deceleration, can force disruptive maneuvers and undermine planning feasibility, posing significant risks [5]–[7]. Like expert drivers who adapt their caution based on perceived intent (e.g., giving more space to aggressive vehicles), autonomous vehicles must interpret and respond to evolving uncertainties online to adaptively maintain safety and efficiency. Yet achieving such a flexible balance remains elusive

in practice: planners that ignore uncertainty can underestimate risks, whereas worst-case formulations become so conservative that efficiency suffers [8]–[10]. Consequently, ensuring the persistent existence of safe trajectories while maintaining high driving efficiency under uncertainty remains an unresolved problem, particularly when adaptive responsiveness to uncertainties is essential.

Stochastic optimization methods, such as chance-constrained approaches, address this problem by permitting small, predefined collision probabilities [11], [12]. However, exact chance constraint evaluation is computationally intractable [13], leading to common approximations with Gaussian uncertainty models [6], [14]. Recent advances, such as chance-constrained nonlinear model predictive control (NMPC) for multi-modal obstacle behaviors [15], ensure recursive feasibility and safety across the entire planning horizon. Nevertheless, these methods still face fundamental limitations: Gaussian approximations struggle to capture the inherently non-Gaussian nature of real-world driving behaviors [16], and even minor constraint violations can lead to hazardous outcomes in unexpected situations. Scenario optimization offers a sampling-based alternative [17], but demands large sample sets to address low-probability, high-risk events, which hinder its practical application in the real world.

To overcome these limitations, robust optimization enforces strict safety by requiring constraint satisfaction under all possible uncertainty realizations within bounded sets [18], [19]. This is typically achieved using forward reachability analysis in motion planning [20], [21]. For example, prior works [8], [22] compute the forward reachable sets (FRSs) for traffic participants while accounting for road network constraints and worst-case control capabilities. Similarly, a robust NMPC framework is designed using HV FRS to guarantee safety under motion uncertainties of the HV [23]. To ensure recursive feasibility, methods such as [24], [25] maintain fail-safe trajectories over infinite horizons, allowing the ego vehicle (EV) to fall back to emergency maneuvers when needed [26]. In [27], a safe backup trajectory is computed using FRS and enforced if the primary stochastic NMPC optimization becomes infeasible. However, sudden transitions to backup trajectories may degrade passenger comfort.

While reachability-based methods offer robust safety guarantees, control barrier function (CBF) provides an alternative approach through forward invariance [28]. The forward invariance of safety sets is closely related to the recursive feasibility for safe trajectories [29], [30], which can be naturally encoded via barrier function constraints [31]. Recent advances integrate reachability analysis with CBFs to certify

Rui Yang, Lei Zheng, and Jun Ma are with The Hong Kong University of Science and Technology, China (e-mail: ryang253@connect.hkust-gz.edu.cn; lzhang135@connect.hkust-gz.edu.cn; jun.ma@ust.hk).

Shuzhi Sam Ge is with the Department of Electrical and Computer Engineering, National University of Singapore, Singapore 117576 (e-mail: samge@nus.edu.sg).

This work has been submitted to the IEEE for possible publication. Copyright may be transferred without notice, after which this version may no longer be accessible.

forward-invariant safety despite uncertainty [32], [33]. For instance, FRS predictions are employed to construct CBFs to handle uncertainties in HV behaviors [34]. While these CBF-based methods provide strong safety guarantees, they often remain overly conservative, especially in dense traffic scenarios, where worst-case assumptions lead to infeasible or inefficient motion plans.

To reduce the conservatism without sacrificing safety, recent research explores learning-based approaches to refine uncertainty estimates. Uncertainty sets are constructed as subsets of worst-case forward reachable space to enable safer yet less conservative planning [35], [36]. When sufficient prior data is available, FRS predictions can be refined through online updates [37], [38]. Learning techniques such as self-supervised neural networks [39], Gaussian processes [40], [41], and active learning [42] show promise, yet often rely on extensive offline training or face challenges in real-time adaptation for multiple HVs. For online learning efficiency, polytopic control-intent sets are learned to predict FRSs of dynamic obstacles [43], while ellipsoidal representations are employed to accelerate computation [44]. However, most of these works do not directly address the recursive feasibility problem under uncertainty. Furthermore, planning solely based on the FRSs of HVs can still be conservative, as it requires a single trajectory to perform well under all possible behaviors.

Complementing these approaches, contingency planning offers a balanced approach by optimizing nominal behavior while maintaining flexibility through backup plans [45], [46]. These methods jointly optimize over a primary horizon for performance and a parallel horizon to handle contingencies [4], [47]. For example, contingency planning is applied to account for model uncertainties and reduce the conservatism of worst-case FRS prediction in [48]. Nevertheless, the non-convex nature of safety requirements in multiple horizons and inherent non-holonomic kinematic constraints poses significant computational challenges for real-time implementation [49]

Recent advances in trajectory optimization for autonomous driving have employed distributed optimization techniques to address the computational bottlenecks. Specifically, the alternating direction method of multipliers (ADMM) is employed to maintain feasibility under constraints while achieving real-time performance [49], [50]. Particularly effective for separable biconvex optimization problems, ADMM-based approaches leverage parallel computing capabilities to facilitate high computational efficiency, enabling rapid response to changing environments [2], [51].

In this study, we propose a real-time contingency trajectory optimization framework that enforces safety through FRS-based barrier functions, with dynamic refinement of HV control-intent sets using event-triggered online learning. This approach ensures feasible, safe trajectories while adaptively managing uncertainty to avoid excessive conservatism. The main contributions of this work are summarized as follows:

- We propose a novel safety-preserving framework for autonomous vehicles, which integrates FRS with discrete barrier functions to ensure robust forward invariance of the safety set. Our method dynamically updates safety constraints through event-triggered online learning of HV

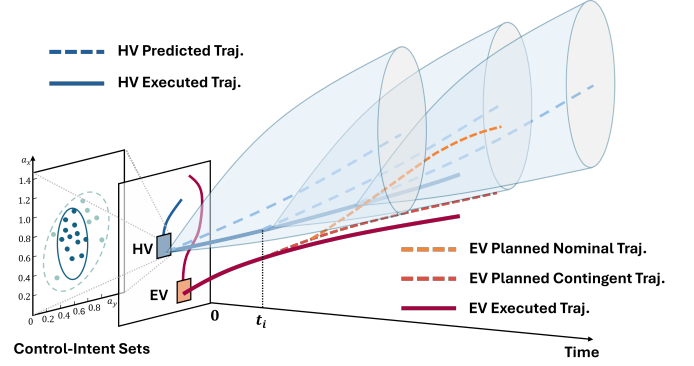


Fig. 1. Overview of the proposed safe contingency trajectory planning framework. The method incrementally refines the control-intent sets of HVs through event-triggered online learning, enabling more accurate FRS predictions (light blue tubes) that adapt to evolving uncertainties in HV behaviors. At each time step t_i , the planner jointly optimizes a nominal performance-driven trajectory and a contingency trajectory enforced by FRS-based barrier constraints, ensuring safety while maintaining comfort and balanced efficiency.

control-intent sets to refine the FRS incrementally. This formulation addresses HV behavioral uncertainty appropriately and ensures collision-free maneuvers without reliance on accurate trajectory predictions.

- We develop a contingency trajectory optimization scheme that ensures safe trajectories with recursive feasibility. By co-optimizing a nominal performance-driven trajectory and a contingency trajectory with FRS-based barrier constraints, it ensures planning outcomes toward regions where safe maneuvers exist. This approach enables defensive driving while maintaining efficiency.
- We leverage the bi-convex structure of the barrier constraints to decompose the non-convex contingency planning problem into tractable QP subproblems using consensus ADMM. This enables efficient computation of feasible trajectories, facilitating rapid response to uncertain driving conditions.
- We validate the proposed approach on synthetic and real-world traffic datasets across different driving scenarios. The results demonstrate its ability to balance safety and efficiency, with improved passenger comfort under uncertain HV behaviors. Real-time performance is further verified through hardware experiments, which underscore its deployability in dynamic and uncertain traffic environments.

The remainder of this paper is structured as follows: Section II introduces the problem statement. Section III discusses event-triggered online learning of HV control-intent sets and FRS prediction, followed by FRS-based safety barrier design. Section IV describes the contingency planning framework and optimization scheme with consensus ADMM, with supporting theoretical analysis. The proposed trajectory planning approach is evaluated in Section V, and a conclusion is drawn in Section VI.

II. PROBLEM STATEMENT

A. System Modeling

We model the motion of the h -th HV's geometric center with a discrete-time integrator for $h \in \mathcal{I}_0^{M-1}$, where M is the total number of HVs in the considered scenario. This formulation facilitates computational tractability while maintaining sufficient accuracy for reachability analysis. With sampling time δT , the dynamics model of the h -th HV at time instant t_i is given by:

$$z_{i+1}^h = Az_i^h + Bu_i^h, \quad (1)$$

where A and B are the state and control matrices, respectively; the state vector $z_i^h = [p_i^{hT} v_i^{hT}]^T \in \mathbb{R}^4$ is composed of position $p_i^h = [p_{x,i}^h p_{y,i}^h]^T$ and velocity $v_i^h = [v_{x,i}^h v_{y,i}^h]^T$, with control input vector $u_i^h = [a_{x,i}^h a_{y,i}^h]^T \in \mathcal{U}^h$ comprising longitudinal and lateral accelerations.

To account for perception inaccuracy, we model the HV state measurement at time t_i as

$$\hat{z}_i^h = z_i^h + \omega_i^h, \quad \|\omega_i^h\|_{\Sigma_\omega^h} \leq 1, \quad (2)$$

where the noise ω_i^h is bounded with known, positive-definite covariance Σ_ω^h .

For the h -th HV, the control capability is defined by two distinct sets: **admissible control set** \mathcal{U}^h , which encompasses all physically feasible control inputs under worst-case constraints, and **control-intent set** $\hat{\mathcal{U}}^h \subseteq \mathcal{U}^h$, encompassing the control inputs the HV is likely to execute within a finite horizon. The admissible set \mathcal{U}^h is assumed known, while the intended set $\hat{\mathcal{U}}^h$ remains unknown *a priori* and should be estimated online through iterative adjustments based on observed behaviors.

To enable smooth trajectory optimization, the state vector $x_i \in \mathcal{X}$ is augmented to include control inputs and their derivatives, defined as:

$$x_i = [p_{x,i} \ p_{y,i} \ \theta_i \ \dot{\theta}_i \ v_i \ a_{x,i} \ a_{y,i} \ j_{x,i} \ j_{y,i}]^T.$$

Here, $p_{x,i}$ and $p_{y,i}$ denote the longitudinal and lateral positions in the global frame, respectively; v_i is the speed; and θ_i is the heading angle. Additionally, $a_{x,i}$ and $a_{y,i}$ are the longitudinal and lateral accelerations, while $j_{x,i}$ and $j_{y,i}$ represent the longitudinal and lateral jerks. Using the yaw rate $\dot{\theta}_i$ and acceleration a_i as control input variables, the EV is modeled as Dubins car with nonholonomic constraints:

$$\begin{aligned} \dot{p}_{x,i} - v_i \cos(\theta_i) &= 0, \\ \dot{p}_{y,i} - v_i \sin(\theta_i) &= 0. \end{aligned} \quad (3)$$

Based on these constraints, we can further derive the following constraint of θ_i and closed-form solution of v_i [52]:

$$\theta_i - \arctan(\dot{p}_{y,i}/\dot{p}_{x,i}) = 0, \quad (4)$$

$$v_i = \sqrt{(\dot{p}_{x,i})^2 + (\dot{p}_{y,i})^2}. \quad (5)$$

B. Problem Statement

This study investigates trajectory optimization for autonomous vehicles in safety-critical environments where M HVs exhibit uncertain behaviors compounded by perception inaccuracies. Complex driving patterns influenced by diverse driving styles and traffic conditions make their trajectories

difficult to predict. To robustly handle the uncertainties, we aim to generate collision-free trajectories by avoiding the reachable regions of HVs, characterized via FRSs over a given time horizon.

Conventional FRSs derived from admissible control sets \mathcal{U}^h tend to be overly conservative, as they account for worst-case actuator limitations. Conversely, using fixed bounds of control inputs may lead to either excessive caution or dangerous underestimation. In reality, the near-future behaviors of an HV are better characterized by the empirical bounds of historical trajectory data, which captures both driving style and traffic conditions [43].

Accordingly, we aim to develop a computationally efficient trajectory optimization framework that enables the EV to accommodate HV uncertainties while ensuring the existence of safe trajectories. Given the EV and HV models in Section II-A, the problem is decomposed into three key subproblems:

- (i) efficiently updating the FRS of HVs (1) by online learning the unknown control-intent sets $\hat{\mathcal{U}}$;
- (ii) formulating barrier constraints using the FRS to enable safe and computationally efficient trajectory optimization;
- (iii) ensuring the feasibility of safe trajectories while balancing safety, efficiency, and passenger comfort.

III. FRS-BASED SAFETY BARRIER

This section introduces the FRS-based discrete barrier function method, addressing the subproblems (i) and (ii) in Section II-B. Section III-A designs the event trigger mechanism for online learning of HV control-intent sets and FRS propagation. Section III-B then formulates the FRS-based safety barrier constraint.

A. FRS Prediction

The FRS rigorously characterizes potential future states for an HV, defined as follows:

Definition 1 (Forward Reachable Set). *The FRS of the h -th HV (1) at the predicted time step k , $k \geq 1$, from an initial state vector z_i is defined as:*

$$\mathcal{R}_{k|i}^h = \left\{ A^k z_i^h + \sum_{j=0}^{k-1} A^{k-1-j} B u_j^h \mid \forall u_j^h \in \hat{\mathcal{U}}^h, j \in \mathcal{I}_0^{k-1} \right\} \quad (6)$$

where the state matrix A and control matrix B are defined in (1), and $\hat{\mathcal{U}}^h$ denotes the control-intent set of the h -th HV.

Following [44], we employ ellipsoidal representations for both the control-intent set and the associated FRS. This ellipsoidal representation supports efficient online learning while simplifying FRS propagation. It also facilitates the construction of safety barrier constraints, improving the computational efficiency for trajectory optimization, as elaborated in Section IV-D.

1) *Event-Triggered Online Learning of Control-Intent Set:* The control-intent set is initialized according to the EV's prior knowledge or assumptions on the HV, and subsequently refined through online learning.

Specifically, at each time step t_i , we obtain the control input vector u_{i-1}^h from the observed state vectors. Then, a control input dataset $\mathcal{C}_i^h = \mathcal{C}_{i-1}^h \cup \{u_{i-1}^h\}$ is maintained for the h -th HV, initialized with \mathcal{C}_0^h , a user-specified estimate of potential HV control inputs.

From an estimation perspective, the elements in \mathcal{C}_i^h can be viewed as the samples drawn from an unknown distribution of $\hat{\mathcal{U}}_i^h$. It is over-approximated using a minimum-volume enclosing ellipsoid of \mathcal{C}_i^h , denoted as:

$$\hat{\mathcal{U}}_i^h = \{u \in \mathbb{R}^2 \mid (u - \mu_{u,i}^h)^T (\Sigma_{u,i}^h)^{-1} (u - \mu_{u,i}^h) \leq 1\}, \quad (7)$$

with an equivalent form $\|P_{u,i}^h u + q_{u,i}^h\|_2 \leq 1$. The parameters $P_{u,i}^h = (\Sigma_{u,i}^h)^{-1/2}$ and $q_{u,i}^h = -P_{u,i}^h \mu_{u,i}^h$ are obtained by solving the following semi-definite programming (SDP) problem [53]:

$$\begin{aligned} \{P_{u,i}^h, q_{u,i}^h\} = \operatorname{argmin}_{\{P, q\}} \quad & \log \det(P^{-1}) \\ \text{s.t.} \quad & \|Pu + q\|_2^2 \leq 1, \quad \forall u \in \mathcal{C}_i^h, \\ & P \in \mathbb{S}_{++}^2. \end{aligned} \quad (8)$$

For large datasets, Khachiyan's algorithm [54] provides efficient computation via first-order approximation. Nevertheless, as the size of \mathcal{C}_i^h increases with the accumulation of control input samples, it introduces computational challenges that hinder real-time implementation. To mitigate these issues, we design the following condition to trigger the updates.

Triggering Condition: The updates occur when

$$t_{m'} = \inf_{i\delta T > t_m} i\delta T \quad (9)$$

such that

$$\|P_{u,m}^h u_{i-1}^h + q_{u,m}^h\|_2^2 \geq 1, \quad (10)$$

where $m, m' \in \mathbb{N}$ denote successive update time instants. Intuitively, when a new control input sample u_{i-1}^h falls outside the current estimated set $\hat{\mathcal{U}}_m^h$, trigger an incremental update such that $\mathcal{C}_i^h \subseteq \hat{\mathcal{U}}_m^h \cup \{u_{i-1}^h\} \subseteq \hat{\mathcal{U}}_{m'}^h$.

Once the triggering condition (10) is satisfied, the parameters $P_{u,m}^h$ and $q_{u,m}^h$ can be incrementally obtained by solving an SDP problem (11) with fixed computational complexity, as formalized in the following lemma:

Lemma 1. [44] *Given the current ellipsoid $\hat{\mathcal{U}}_m^h$ and a new sample u_{i-1}^h , the updated parameters $\{P_{u,m'}^h, q_{u,m'}^h\}$ of the minimum-volume enclosing ellipsoid $\hat{\mathcal{U}}_{m'}^h$ are computed to satisfy $\hat{\mathcal{U}}_m^h \cup \{u_{i-1}^h\} \subseteq \hat{\mathcal{U}}_{m'}^h$ via:*

$$\begin{aligned} \min_{S, c, \lambda_j} \quad & \log \det(S^{-1}) \\ \text{s.t.} \quad & \begin{bmatrix} S - \lambda_j H_j & c - \lambda_j \zeta_j & 0 \\ (c - \lambda_j \zeta_j)^T & -1 - \lambda_j n_j & c^T \\ 0 & c & -S \end{bmatrix} \preceq 0, \quad j \in \{1, 2\}, \end{aligned} \quad (11)$$

where $H_1 = (P_m^h)^T P_m^h$, $\zeta_1 = (P_m^h)^T q_m^h$, $n_1 = \|q_m^h\|_2^2 - 1$; and $H_2 = I_2$, $\zeta_2 = -u_m^h$, $n_2 = \|u_m^h\|_2^2 - \epsilon$. Here, $I_2 \in \mathbb{R}^{2 \times 2}$ is the identity matrix, and $\epsilon > 0$. The optimal solution yields the updated ellipsoid parameters:

$$P_{u,m'}^h = (S^*)^{-1/2}, \quad q_{u,m'}^h = (S^*)^{1/2} c^*. \quad (12)$$

Corollary 1. *For all $t_i \in [t_m, t_{m'})$, the control input vector satisfies $u_i^h \in \hat{\mathcal{U}}_m^h$.*

Remark 1. *The online learning mechanism (9)-(12) ensures compatibility with worst-case analysis by requiring that the initial control-intent set \mathcal{C}_0^h includes the worst-case control inputs for the h -th HV.*

2) *FRS Propagation:* Using the learned control-intent set $\hat{\mathcal{U}}_m^h$, we propagate the FRSs over the prediction horizon N , starting at time step $t_i \geq t_m$.

Considering perception noise, the initial FRS is given by:

$$\mathcal{R}_{0|i}^{h,z} = \{z \in \mathbb{R}^4 \mid (z - \tilde{z}_i^h)^\top (\Sigma_{z,0|i}^h)^{-1} (z - \tilde{z}_i^h) \leq 1\}, \quad (13)$$

where $\Sigma_{z,0|i}^h = \Sigma_\omega^h$.

Then, the FRS $\mathcal{R}_{k|i}^{h,z}$ at predicted time step k starting from t_i is computed recursively:

$$\mathcal{R}_{k|i}^{h,z} = A \mathcal{R}_{k-1|i}^{h,z} \oplus B \hat{\mathcal{U}}_m^h, \quad k \in \mathcal{I}_1^N. \quad (14)$$

Although $\mathcal{R}_{0|i}^{h,z}$ and $\hat{\mathcal{U}}_m^h$ are ellipsoids, their Minkowski sum $\mathcal{R}_{k|i}^{h,z}$ is typically not an ellipsoid [55]. We therefore construct an efficient ellipsoidal over-approximation:

$$\hat{\mathcal{R}}_{k|i}^{h,z} = \{z \in \mathbb{R}^4 \mid (z - \mu_{z,k|i}^h)^T (\hat{\Sigma}_{z,k|i}^h)^{-1} (z - \mu_{z,k|i}^h) \leq 1\},$$

with parameters $(\mu_{z,k|i}^h, \hat{\Sigma}_{z,k|i}^h)$ given by:

$$\mu_{z,k|i}^h = A \mu_{z,k-1|i}^h + B \mu_{u,m}^h, \quad (15)$$

$$\hat{\Sigma}_{z,k|i}^h = \kappa (\tilde{\Sigma}_{z,k-1|i}^h / \rho_{z,k-1|i} + \tilde{\Sigma}_{u,m}^h / \rho_{u,m}), \quad (16)$$

where $\tilde{\Sigma}_{z,k-1|i}^h = A \tilde{\Sigma}_{z,k-1|i}^h A^T$; $\tilde{\Sigma}_{u,m}^h = B \Sigma_{u,m}^h B^T + \epsilon_2 I_4$; and directional scaling factors $\rho_{z,k-1|i} = \sqrt{l^T \tilde{\Sigma}_{z,k-1|i}^h l}$, $\rho_{u,m} = \sqrt{l^T \tilde{\Sigma}_{u,m}^h l}$, $\kappa = \rho_{z,k-1|i} + \rho_{u,m}$ are computed along direction l .

3) *Occupancy Prediction:* Based on the FRS prediction, the positional occupancy $\mathcal{R}_{k|i}^h = \text{Proj}_{\text{position}}(\hat{\mathcal{R}}_{k|i}^{h,z})$ is obtained via projection:

$$\mathcal{R}_{k|i}^h = \{p \in \mathbb{R}^2 \mid (p - \mu_{p,k|i}^h)^T (\hat{\Sigma}_{p,k|i}^h)^{-1} (p - \mu_{p,k|i}^h) \leq 1\}. \quad (17)$$

However, considering only the HV center while neglecting the geometry is insufficient for safety assurance. Therefore, we employ an ellipsoidal geometry set to explicitly account for the full shape characteristics of both the HV and EV, which is represented by $\mathcal{D}_{safe} = \{p \in \mathbb{R}^2 \mid p^T (\Sigma_{safe}^h)^{-1} p \leq 1\}$. Its lengths of major and minor axes are denoted as l_x^h and l_y^h , respectively.

Thus, the complete HV FRS occupancy can be derived as an external ellipsoidal approximation of $\mathcal{R}_{k|i}^h \oplus \mathcal{D}_{safe}$, denoted by:

$$\hat{\mathcal{R}}_{k|i}^h = \{p \in \mathbb{R}^2 \mid (p - \mu_{p,k|i}^h)^T (\hat{\Sigma}_{p,k|i}^h)^{-1} (p - \mu_{p,k|i}^h) \leq 1\}, \quad (18)$$

where $\mu_{p,k|i}^h = [\mu_{x,k|i}^h \ \mu_{y,k|i}^h]^T$ denotes the center of the positional occupancy $\mathcal{R}_{k|i}^h$. The ellipsoidal approximation can be computed similarly to (15) and (16). We denote the lengths

of major and minor axes of the ellipsoid $\hat{\mathcal{R}}_{k|i}^h$ as $l_{x,k|i}^h$ and $l_{y,k|i}^h$, respectively.

Remark 2. In practice, the bound of noise in (2) can be estimated via a variety of filtering techniques (e.g., Kalman filter). The estimation covariance quantifies perception uncertainties, which can be integrated into the initial FRS. By conservatively tuning the filter parameters and confidence level, the resulting FRS robustly contains the true state, enabling reliable collision checking.

Remark 3. The initial control-intent set encodes the EV's a priori knowledge of HV behaviors and implicitly determines the basic conservatism of the planning framework. The system adapts dynamically through event-triggered learning, refining these sets based on observed behaviors, thus improving prediction accuracy over time.

Let $\hat{\mathcal{O}}_{k|i}^h = z_{p,k|i}^h \oplus \mathcal{D}_{\text{safe}}$ denote the predicted positional occupancy at predicted time step k from t_i , with $z_{p,k|i}^h = [z_{x,k|i}^h z_{y,k|i}^h]^T$ denoting the position vector, while $\mathcal{O}_{k|i}^h$ represents the actual positional occupancy at time instant t_{i+k} .

Lemma 2. Consider control input vectors of the h -th HV during planning horizon N satisfying $u_{k|i}^h \in \hat{\mathcal{U}}_m^h, \forall k \in \mathcal{I}_0^{N-1}$, for all $t_i \in [t_m, t_{m'} - N)$, then the following containment relations hold:

$$\mathcal{O}_{k|i}^h \subseteq \hat{\mathcal{R}}_{k|i}^h, \forall k \in \mathcal{I}_0^N \quad \text{and} \quad \hat{\mathcal{R}}_{k|i+1}^h \subseteq \hat{\mathcal{R}}_{k+1|i}^h, \forall k \in \mathcal{I}_0^{N-1}.$$

Proof. The initial FRS $\mathcal{R}_{0|i}^{h,z}$ in (13) is an ellipsoid centered at the estimated HV state vector \hat{z}_i^h with covariance $\Sigma_{z,0}^h$, which ensures $z_{0|i}^h = z_i^h \in \mathcal{R}_{0|i}^{h,z}$. Since $u_{k|i}^h \in \hat{\mathcal{U}}_m^h$ for all $k \in \mathcal{I}_0^{N-1}$, the recursive propagation in (14) ensure containment of the true state trajectory within the FRSs as well as their over-approximations: $z_{k|i}^h \in \mathcal{R}_{k|i}^{h,z} \subseteq \hat{\mathcal{R}}_{k|i}^h$.

Projecting $\hat{\mathcal{R}}_{k|i}^{h,z}$ to positional space via (17) preserves this containment, yielding $z_{p,k|i}^h \in \mathcal{R}_{k|i}^h$ for all $k \in \mathcal{I}_0^N$.

Incorporating the vehicle geometry $\mathcal{D}_{\text{safe}}$ through Minkowski sum and its ellipsoidal approximation ensures $z_{p,k|i}^h \oplus \mathcal{D}_{\text{safe}} \subseteq \mathcal{R}_{k|i}^h \oplus \mathcal{D}_{\text{safe}}$. Following the over-approximation property of the external ellipsoid, $\mathcal{O}_{k|i}^h \subseteq \hat{\mathcal{R}}_{k|i}^h$ holds for all $k \in \mathcal{I}_0^N$.

With the initial condition $z_{p,0|i+1}^h \in \hat{\mathcal{R}}_{0|i+1}^h \subseteq \hat{\mathcal{R}}_{1|i}^h$, the ellipsoidal approximation preserves the containment relationship $\hat{\mathcal{R}}_{k|i+1}^h \subseteq \hat{\mathcal{R}}_{k+1|i}^h, \forall k \in \mathcal{I}_0^{N-1}$. \square

B. FRS-Based Safety Barrier

The safe set can be characterized by a sublevel set of a continuously differentiable function \mathcal{B} :

$$\mathcal{F}(\mathcal{O}^h) = \{x_i \in \mathcal{X} \mid \mathcal{B}(x_i, \mathcal{O}^h) \geq 0\} \quad (19)$$

Definition 2 (Forward Invariance). The set $\mathcal{F}(\mathcal{O}^h)$ is forward invariant if for any initial state vector $x_0 \in \mathcal{F}(\mathcal{O}^h)$, the condition $\mathcal{B}(x_i, \mathcal{O}^h) \geq 0$ holds for all $i \geq 0$.

Lemma 3. [56, Proposition 4] The safe set $\mathcal{F}(\mathcal{O}^h)$ is forward invariant, if \mathcal{B} with initial condition $\mathcal{B}(x_0, \mathcal{O}^h) \geq 0$ satisfies:

$$\Delta \mathcal{B}(x_i, \mathcal{O}^h) + \alpha \mathcal{B}(x_i, \mathcal{O}^h) \geq 0, \quad (20)$$

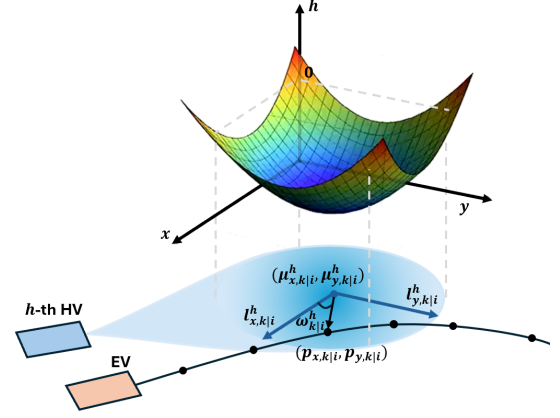


Fig. 2. Illustration of the FRS-based safety barrier. At predicted time step k starting from t_i , the trajectory point $p_{k|i}$ of the EV is pushed away from the FRS positional occupancy prediction of the HV, along the direction $\omega_{k|i}^h$. The safe set $\mathcal{F}(\hat{\mathcal{R}}_{k|i}^h)$ (outside the ellipsoid) is encoded using discrete barrier function $\mathcal{B} \geq 0$.

where $\Delta \mathcal{B}(x_i, \mathcal{O}^h) = \mathcal{B}(x_{i+1}, \mathcal{O}^h) - \mathcal{B}(x_i, \mathcal{O}^h)$, $0 < \alpha \leq 1$, and \mathcal{B} is said to be a discrete-time barrier function.

Following the methodology in [2], we employ polar coordinate transformations to formulate the nominal **deterministic safety barrier constraints** for collision avoidance as:

$$\begin{cases} p_{x,k|i} = z_{x,k|i}^h + l_x^h d_{k|i}^h \cos(\omega_{k|i}^h), \\ p_{y,k|i} = z_{y,k|i}^h + l_y^h d_{k|i}^h \sin(\omega_{k|i}^h), \\ \Delta \mathcal{B}(x_{k|i}, \hat{\mathcal{O}}_{k|i}^h) + \alpha \mathcal{B}(x_{k|i}, \hat{\mathcal{O}}_{k|i}^h) \geq 0, k \in \mathcal{I}_0^{N-1}. \end{cases} \quad (21)$$

Here, the parameters l_x^h and l_y^h represent the semi-axes of the ellipsoidal safety boundary, and barrier function \mathcal{B} is defined as $\mathcal{B}(x_{k|i}, \hat{\mathcal{O}}_{k|i}^h) = d_{k|i}^h(x_{k|i}, \hat{\mathcal{O}}_{k|i}^h) - 1$, where $d_{k|i}^h$ is the Mahalanobis distance from $x_{k|i}$ to the ellipsoid $\hat{\mathcal{O}}_{k|i}^h$. Intuitively, when a trajectory point $[p_{x,k|i} p_{y,k|i}]^T$ of the EV penetrates the obstacle region centered at $[z_{x,k|i}^h z_{y,k|i}^h]^T$, it is pushed outward along an optimal repulsion direction $\omega_{k|i}^h$:

$$\omega_{k|i}^h = \arctan \left(\frac{l_x^h (p_{y,k|i} - z_{y,k|i}^h)}{l_y^h (p_{x,k|i} - z_{x,k|i}^h)} \right) \quad (22)$$

Note that the constraint (21) characterizes the collision avoidance by maintaining a minimum safety margin throughout the planning horizon, with an equivalent polar coordinate formulation:

$$d_{k+1|i}^h - 1 - (1 - \alpha)(d_{k|i}^h - 1) \geq 0. \quad (23)$$

However, since accurate trajectory prediction of HVs are typically unavailable, we utilize the obtained ellipsoid FRS occupancy $\hat{\mathcal{R}}_{k|i}^h$ to construct the **FRS-based safety barrier constraints** as shown in Fig. 2, which is derived as:

$$\begin{cases} p_{x,k|i} = \mu_{x,k|i}^h + l_{x,k|i}^h d_{k|i}^h \cos(\omega_{k|i}^h), \\ p_{y,k|i} = \mu_{y,k|i}^h + l_{y,k|i}^h d_{k|i}^h \sin(\omega_{k|i}^h), \\ \Delta \mathcal{B}(x_{k|i}, \hat{\mathcal{R}}_{k|i}^h) + \alpha \mathcal{B}(x_{k|i}, \hat{\mathcal{R}}_{k|i}^h) \geq 0, k \in \mathcal{I}_0^{N-1}. \end{cases} \quad (24)$$

The barrier function introduces a fundamental duality principle that a larger obstacle region induces a smaller safe set.

Lemma 4. Let $\hat{\mathcal{R}}_A$ and $\hat{\mathcal{R}}_B$ be two ellipsoidal sets in \mathbb{R}^2 with centers z_A, z_B and positive definite shape matrices Q_A, Q_B , respectively. The following containment relationship holds:

$$\hat{\mathcal{R}}_A \subseteq \hat{\mathcal{R}}_B \implies \mathcal{F}(\hat{\mathcal{R}}_B) \subseteq \mathcal{F}(\hat{\mathcal{R}}_A),$$

Proof. For any $x \in \mathcal{F}(\hat{\mathcal{R}}_B)$, the Mahalanobis distance satisfies $d(x, \hat{\mathcal{R}}_B) = \|x - z_B\|_{Q_B^{-1}} \geq 1$. The containment $\hat{\mathcal{R}}_A \subseteq \hat{\mathcal{R}}_B$ implies $\{x \mid \|x - z_A\|_{Q_A^{-1}} \leq 1\} \subseteq \{x \mid \|x - z_B\|_{Q_B^{-1}} \leq 1\}$. Consequently, for $x \notin \text{Int}(\hat{\mathcal{R}}_B)$, we have $\|x - z_A\|_{Q_A^{-1}} \geq 1$. Thus, $d(x, \hat{\mathcal{R}}_A) - 1 \geq 0$, with equality only for $x \in \partial\hat{\mathcal{R}}_A$. Therefore, it gives $x \in \mathcal{F}(\hat{\mathcal{R}}_A)$, and this completes the proof. \square

It can be shown that the $\mathcal{F}(\hat{\mathcal{R}}_{k|i}^h)$ is a robust safe set of the EV with respect to the h -th HV.

Lemma 5. Let the h -th HV satisfies $u_{k|i}^h \in \hat{\mathcal{U}}_m^h$. The EV trajectory with an initial state vector $x_{k|i} \in \mathcal{F}(\hat{\mathcal{R}}_{k|i}^h)$ can robustly avoid collisions $x_{k+1|i} \in \mathcal{F}(\hat{\mathcal{R}}_{k+1|i}^h) \subseteq \mathcal{F}(\mathcal{O}_{k+1|i}^h)$, $\forall k \geq 0$ for all realizable trajectories of the HV, if the barrier condition (24) is satisfied.

Proof. Since the initial state vector $x_{k|i} \in \mathcal{F}(\hat{\mathcal{R}}_{k|i}^h)$, we have $\mathcal{B}(x_{k|i}, \hat{\mathcal{R}}_{k|i}^h) \geq 0$ according to (19). From (20), one can derive $\mathcal{B}(x_{k+1|i}, \hat{\mathcal{R}}_{k+1|i}^h) \geq (1 - \alpha)\mathcal{B}(x_{k|i}, \hat{\mathcal{R}}_{k|i}^h) \geq 0$. Thus, $x_{k+1|i} \in \mathcal{F}(\hat{\mathcal{R}}_{k+1|i}^h)$. Since $\mathcal{O}_{k+1|i}^h \subseteq \hat{\mathcal{R}}_{k+1|i}^h$ holds for control input vectors $u_{k|i}^h \in \hat{\mathcal{U}}_m^h$ by Lemma 2, we have $\mathcal{F}(\hat{\mathcal{R}}_{k+1|i}^h) \subseteq \mathcal{F}(\mathcal{O}_{k+1|i}^h)$ according to Lemma 4. Consequently, $x_{k+1|i} \in \mathcal{F}(\hat{\mathcal{R}}_{k+1|i}^h) \subseteq \mathcal{F}(\mathcal{O}_{k+1|i}^h)$ holds. \square

IV. SAFE CONTINGENCY TRAJECTORY OPTIMIZATION

In this section, we first introduce the trajectory representation based on Bézier curves for smoothness and computational efficiency. Next, we formulate a contingency optimization problem with FRS-based safety barrier constraints to enforce safety. Finally, leveraging the biconvex structure of the optimization problem, we derive an equivalent reformulation that enables efficient alternating optimization using ADMM.

A. Trajectory Parameterization

We employ Bézier curves to parameterize EV trajectories over a finite duration of T . This representation exploits the hodograph property to directly constrain higher-order derivatives, ensuring dynamical feasibility [57]. A degree- n Bézier curve is constructed using $(n + 1)$ control points over a normalized interval $\nu \in [0, 1]$:

$$b(\nu) = \sum_{j=0}^n c_j b_{j,n}(\nu) = c^T \mathcal{B}_v(\nu),$$

where $c = [c_0 \dots c_n]^T \in \mathbb{R}^{n+1}$ are control points, $\mathcal{B}_v(\nu) = [b_{0,n}(\nu) \dots b_{n,n}(\nu)]^T \in \mathbb{R}^{n+1}$ consists of Bernstein polynomial basis $b_{j,n}(\nu) = \binom{n}{j} \nu^j (1 - \nu)^{n-j}$, and $\nu = (t - t_i)/T \in [0, 1]$ is the normalized time. Discrete-time points are obtained as:

$$b_k = c^T \mathcal{B}_k,$$

where $\mathcal{B}_k = \mathcal{B}_v(k\delta T)$, and $\delta T = T/N$ is the fixed time step.

The state vector of EV can then be parameterized as:

$$x_{k|i} = \mathbf{p}(c_x, c_y, c_\theta).$$

Specifically, three distinct Bézier curves are used to represent the longitudinal displacement, lateral displacement and heading angle, which are denoted by $p_{x,k|i} = c_x^T \mathcal{B}_k$, $p_{y,k|i} = c_y^T \mathcal{B}_k$, and $p_{\theta,k|i} = c_\theta^T \mathcal{B}_k$, respectively, with corresponding control points c_x, c_y , and c_θ . Higher-order derivatives follow from the hodograph property: $\dot{\theta}_{k|i} = c_\theta^T \dot{\mathcal{B}}_k$, $v_{k|i} = (c_x^T \dot{\mathcal{B}}_k + c_y^T \ddot{\mathcal{B}}_k)^{\frac{1}{2}}$, $a_{x,k|i} = c_x^T \ddot{\mathcal{B}}_k$, $a_{y,k|i} = c_y^T \ddot{\mathcal{B}}_k$, $j_{x,k|i} = c_x^T \ddot{\mathcal{B}}_k$, and $j_{y,k|i} = c_y^T \ddot{\mathcal{B}}_k$.

B. Safe Contingency Trajectory Optimization

We formulate a trajectory optimization problem through simultaneous optimization of a nominal trajectory and a contingency trajectory constrained by FRS-based safety barriers. For clarity, the following formulations are presented for an arbitrary HV indexed by $h \in \mathcal{I}_0^{M-1}$, with all h -indexed quantities defined per-HV and naturally extendable to all M HVs.

While more accurate prediction methods exist [58], we intentionally employ a constant-velocity model to explicitly demonstrate the robustness to prediction errors. Notably, our framework works with any HV prediction method as long as the predicted states meet this basic containment condition:

Assumption 1. The predicted HV position occupancy $\hat{\mathcal{O}}_{k|i}^h$ is contained within the predicted FRS position occupancy:

$$\hat{\mathcal{O}}_{k|i}^h \in \hat{\mathcal{R}}_{k|i}^h, \quad \forall k \in \mathcal{I}_0^N.$$

This assumption is enforceable because the HV prediction method can be systematically designed to ensure containment through proper control constraint characterization. It is trivially satisfied under constant-velocity prediction due to the conservative nature of FRS propagation.

The optimization problem at t_i is formulated as:

$$\min_{\{c_x^r, c_y^r, c_\theta^r, c_x^s, c_y^s, c_\theta^s\}} \mathcal{J} \quad (25a)$$

$$\text{s.t. } x_{0|i}^r = x(t_i), \quad x_{0|i}^s = x(t_i), \quad (25b)$$

$$x_{k|i}^r \in \mathcal{X}, \quad x_{k|i}^s \in \mathcal{X} \quad (25c)$$

$$x_{N|i}^r \in \mathcal{X}_f, \quad x_{N|i}^s \in \mathcal{X}_f \quad (25d)$$

$$x_{k+1|i}^r = f(x_{k|i}^r), \quad (25e)$$

$$x_{k+1|i}^s = f(x_{k|i}^s), \quad (25f)$$

$$x_{k|i}^r = \mathbf{p}(c_x^r, c_y^r, c_\theta^r), \quad (25g)$$

$$x_{k|i}^s = \mathbf{p}(c_x^s, c_y^s, c_\theta^s), \quad (25h)$$

$$x_{k|i}^r \text{ satisfies (21)}, \quad (25i)$$

$$x_{k|i}^s \text{ satisfies (24)}, \quad (25j)$$

$$\varphi(x_{l|i}^r) = \varphi(x_{l|i}^s), \quad l \in \mathcal{I}_0^{N_s-1}, \quad (25k)$$

$$\forall k \in \mathcal{I}_0^{N-1}.$$

Here, x_k^r and x_k^s represent the state vectors for the nominal and safe contingency trajectories, respectively, with corresponding control points c_x^r, c_y^r, c_θ^r , and c_x^s, c_y^s, c_θ^s . $x(t_i)$ denotes current

state vector of the EV at t_i . The function $f(\cdot)$ implements the kinematic constraint (3).

The objective function \mathcal{J} combines the desired lateral position $p_{y,d}$ and longitudinal speed $v_{x,d}$ with trajectory smoothness, expressed as:

$$\begin{aligned} \mathcal{J} = & (1 - p_s) \sum_{k=0}^{N-1} w_x^r (c_x^r)^T c_x^r)^2 + w_y^r (c_y^r)^T c_y^r)^2 + w_\theta^r (c_\theta^r)^T c_\theta^r)^2 \\ & + w_{v,d}^r (c_x^r)^T \dot{B}_k - v_{x,d})^2 + w_{y,d}^r (c_y^r)^T B_k - p_{y,d})^2 \\ & + p_s \sum_{k=0}^{N-1} w_x^s (c_x^s)^T c_x^s)^2 + w_y^s (c_y^s)^T c_y^s)^2 + w_\theta^s (c_\theta^s)^T c_\theta^s)^2 \\ & + w_{v,d}^s (c_x^s)^T \dot{B}_k - v_{x,d})^2 + w_{y,d}^s (c_y^s)^T B_k - p_{y,d})^2, \end{aligned} \quad (26)$$

where the weights p_s , w_x^r , w_y^r , w_θ^r , $w_{v,d}^r$, $w_{y,d}^r$, w_x^s , w_y^s , w_θ^s , $w_{v,d}^s$, and $w_{y,d}^s$ are all positive constants.

The two parallel trajectories share the same dynamics inherent in the hodograph property of the Bézier curve (25g)-(25h), initial conditions (25b), terminal state constraints (25d) with terminal state set \mathcal{X}_f , and kinematic constraints as stated in (25e)-(25f). We tie them together by requiring the initial segments of length N_s , $N_s \leq N$, to be consistent (25k). For safety assurance, the state vectors x_k^r over the nominal horizon are required to remain within the safe state set with respect to the HV predictions $\hat{\mathcal{O}}_k^h$, as stated in (25i). To handle behavioral uncertainty, we impose the FRS-based safety barrier (25j) as safeguards against possible HV behaviors in the contingency horizon.

The weighting parameter p_s balances nominal planning and contingency handling via FRS-based barrier constraints and can be adjusted according to the desired level of conservatism. The contingency planning formulation in (25) minimizes the expected cost over both trajectories. As prediction confidence increases, smaller values of p_s can be used. This approach generates a nominal trajectory based on prediction $\hat{\mathcal{O}}_k(\cdot)$ while consistently maintaining a safe contingency plan.

C. Planning-Horizon Configurations with Formal Guarantees

We analyze two standard planning-horizon configurations used by the proposed planning framework: a *shrinking horizon* and a *receding horizon*. The former captures short, goal-directed maneuvers that must complete within a known mission duration (e.g., mandated lane change to reach an exit, controlled stop into a refuge bay). It also serves as a safety mode should perception temporarily fail. The latter reflects the normal navigation regime in which fresh predictions and FRS updates arrive as time advances.

Shrinking-Horizon Configuration: Let N_{SH} denote the total number of mission steps remaining at t_0 . At generic time step index i with current time t_i , the optimization horizon in (25a) is chosen to span the *remaining* mission duration:

$$N = N_{SH} - i. \quad (27)$$

This configuration is appropriate when the EV must guarantee completion of a finite-time maneuver under bounded uncertainty without relying on future FRS updates.

We next establish that, under mild conditions, feasibility and safety propagate forward as the horizon shrinks.

Theorem 1 (Shrinking-Horizon Recursive Feasibility and Safety). *Suppose: (i) no HV FRS update events are triggered over the finite mission interval $[t_0, t_{N_{SH}}]$; and (ii) Problem (25) with horizon (27) is feasible at t_0 for Bézier curve order $n \geq N_{SH} - 1$ and barrier coefficient $\alpha = 1$. Then the following hold for every $t_i \leq t_{N_{SH}}$:*

- 1) **Recursive Feasibility:** Problem (25) with horizon (27) remains feasible.
- 2) **Open-Loop Safety:** The contingency trajectory satisfies $x_{k|i}^s \in \mathcal{F}(\hat{\mathcal{O}}_{k|i}^h)$ for all $k \in \mathcal{I}_0^{N_{SH}-i}$.
- 3) **Closed-Loop Safety:** The executed trajectory $\{x_i\}_{i=0}^{N_{SH}}$ satisfies $x_i \in \mathcal{F}(\hat{\mathcal{O}}_i^h)$ at each time step.

Proof. Let $\{x_{0|i}^{r*}, \dots, x_{N_{SH}-i|i}^{r*}\}$ and $\{x_{0|i}^{s*}, \dots, x_{N_{SH}-i|i}^{s*}\}$ denote the optimal nominal and contingency state sequences obtained from (25) at time t_i . Form a *shifted candidate* sequence for the problem at the next time t_{i+1} :

$$x_{k|i+1} = x_{k+1|i}^{s*}, \quad k \in \mathcal{I}_0^{N_{SH}-i-1}.$$

That is, we drop the first state vector of the contingency trajectory and reuse its suffix for both branches in the new problem. Thus, the candidate sequence satisfies the initial condition (25b), state constraint (25c), terminal state constraint (25d), and kinematics constraints (25e)-(25f). Also, the identity of two branches implies the consensus constraint (25k) holds trivially.

From Lemma 2 we have one-step containment relation $\hat{\mathcal{R}}_{k|i+1} \subseteq \hat{\mathcal{R}}_{k+1|i}$ for $k \in \mathcal{I}_0^{N_{SH}-i-1}$. By Lemma 4, the associated safe sets are reversely contained: $\mathcal{F}(\hat{\mathcal{R}}_{k|i+1}) \supseteq \mathcal{F}(\hat{\mathcal{R}}_{k+1|i})$. Since $x_{k+1|i}^{s*} \in \mathcal{F}(\hat{\mathcal{R}}_{k+1|i})$ is satisfied at time t_i , it follows that $x_{k|i+1} \in \mathcal{F}(\hat{\mathcal{R}}_{k|i+1})$. In other words, $\mathcal{B}(x_{k|i+1}, \hat{\mathcal{R}}_{k|i}^h) \geq 0$, satisfying FRS-based barrier constraint (25j) again with $\alpha = 1$.

Since we have $\hat{\mathcal{O}}_{k|i+1}^h \subseteq \hat{\mathcal{R}}_{k|i+1}^h$ under Assumption 1, we have $x_{k|i+1} \in \mathcal{F}(\hat{\mathcal{R}}_{k|i+1}^h) \subseteq \mathcal{F}(\hat{\mathcal{O}}_{k|i+1}^h)$, $\forall k \in \mathcal{I}_0^{N_{SH}-i}$. It means the nominal safety constraint (25i) is satisfied with $\mathcal{B}(x_{k|i+1}, \hat{\mathcal{O}}_{k|i}^h) \geq 0$ with $\alpha = 1$.

According to Corollary 1, the actual HV control inputs up to the next update time remain contained in the learned control-intent sets. Thus, the actual HV occupancy $\mathcal{O}_{k|i+1}^h$ is contained in $\hat{\mathcal{R}}_{k|i+1}^h$, preserving the safety of open-loop trajectory, $x_{k|i+1} \in \mathcal{F}(\hat{\mathcal{R}}_{k|i+1}^h) \subseteq \mathcal{F}(\mathcal{O}_{k|i+1}^h)$, $\forall k \in \mathcal{I}_0^{N_{SH}-i-1}$. Since the closed-loop system executes the first state vector of the planned trajectory at each iteration, thus safety of the closed-loop trajectory is also satisfied, $x_i = x_{0|i} \in \mathcal{F}(\mathcal{O}_{0|i}^h) = \mathcal{F}(\hat{\mathcal{O}}_i^h)$.

Let $P_x = [p_{x,1|i}^{s*}, \dots, p_{x,N_{SH}-i|i}^{s*}]^T$ collect the longitudinal components of the shifted contingency sequence, and analogously for P_y and P_θ . Let $\mathcal{B} = [\mathcal{B}_1 \dots \mathcal{B}_{N_{SH}-i}] \in \mathbb{R}^{(n+1) \times (N_{SH}-i)}$ denote the Bernstein basis evaluation matrix; $n \geq N_{SH} - 1$ implies \mathcal{B} has full column rank, so the minimum-norm pseudoinverse yields control points $c_x^{s*} = \mathcal{B}^\dagger P_x$ that reproduce the candidate trajectory. Repeating each component gives valid Bézier parameterizations satisfying (25g)-(25h).

This establishes recursive feasibility and both safety properties at t_{i+1} . Induction on i completes the proof. \square

Receding-Horizon Configuration: For routine navigation in dynamic environments, we employ a fixed horizon:

$$N = N_{\text{RH}} \quad (28)$$

which shifts forward one step at each planning instant. This allows continuous incorporation of updated HV intent and FRS information and is the standard operating mode of our framework.

Assumption 2. The terminal state set \mathcal{X}_f is forward invariant for the EV under a designated fallback policy (e.g., controlled braking), ensuring $\mathcal{X}_f \subseteq \mathcal{F}(\hat{\mathcal{R}}_{k|i}^h), \forall k \geq N$, with the HV FRS positional occupancy beyond the prediction horizon.

Remark 4. Assumption 2 reflects the practical impossibility of predicting HV intent arbitrarily far ahead in mixed traffic. Consequently, we assume that HVs beyond the horizon will not engage in excessively irrational or deliberately adversarial maneuvers that would preclude the forward invariance of the terminal state set. The forward invariance can be enforced by properly employing a well-designed fallback policy, such as controlled braking, with the barrier constraints as established in Lemma 3. Similar set invariance conditions are widely adopted in model predictive control literature to guarantee recursive feasibility [29], [30], [48].

Theorem 2 (Receding-Horizon Recursive Feasibility and Safety). Suppose: (i) the interval between successive HV FRS update events exceeds the planning horizon, i.e., $t_{m'} > t_{m+N}$; and (ii) Problem (25) with horizon (28) is feasible at t_m for Bézier curve order $n \geq N_{\text{RH}}$ and $\alpha = 1$. Then for every $t_i \in [t_m, t_{m'+N}]$, the following hold:

- 1) **Recursive Feasibility:** Problem (25) remains feasible.
- 2) **Open-Loop Safety:** The contingency trajectory satisfies $x_{k|i}^s \in \mathcal{F}(\mathcal{O}_{k|i}^h)$ for all $k \in \mathcal{I}_0^N$.
- 3) **Closed-Loop Safety:** The executed trajectory satisfies $x_i \in \mathcal{F}(\mathcal{O}_i^h)$ at each time step.

Proof. Let $\{x_{0|i}^{r*}, \dots, x_{N|i}^{r*}\}$ and $\{x_{0|i}^{s*}, \dots, x_{N|i}^{s*}\}$ denote the optimal nominal and contingency state sequences obtained from (25) at time t_i . The argument generalizes the proof of Theorem 1 with the following additions.

Under Assumption 2, there exists a state vector $x_{N+1|i}^{s*} \in \mathcal{X}_f \subseteq \mathcal{F}(\hat{\mathcal{R}}_{N+1|i}^h)$ satisfying the kinematic constraint (25f). At time instant t_{i+1} , we consider

$$x_{k|i+1} = x_{k+1|i}^{s*}, \quad k \in \mathcal{I}_0^N.$$

as a trajectory candidate for both nominal and contingency branches. Since the predicted HV FRS position occupancy beyond horizon N remains constant at time instant t_i , $x_{N+1|i}^{s*} \in \mathcal{F}(\hat{\mathcal{R}}_{N+1|i}^h) \subseteq \mathcal{F}(\hat{\mathcal{R}}_{N|i+1}^h)$, so the FRS-based barrier constraint (25j) holds one step later, i.e., $x_{k|i+1} \in \mathcal{F}(\hat{\mathcal{R}}_{k|i+1}^h)$ for all $k \in \mathcal{I}_0^N$. Lemma 2 and Lemma 4 propagate the remaining steps exactly as in the shrinking-horizon case. Also, the control points of Bézier curves that reproduce the candidate trajectories can be computed following the same way. \square

Remark 5. While the assumption $n \geq N_{\text{RH}}$ (or $n \geq N_{\text{SH}} - 1$ in Theorem 1) streamlines the proof algebraically, high-order Bézier curves are generally not desirable in practice due

to their tendency to exhibit oscillatory behavior, which can induce control chattering and numerical instabilities [57]. Instead, trajectories are typically constructed as piecewise low-order Bézier segments with continuity constraints at junctions. Crucially, the recursive feasibility guarantee can be easily extended to remain valid with proper trajectory parameterization. This depends primarily on the horizon-shifting mechanism and the properties of the invariant safety barrier constraints in the contingency mechanism.

Remark 6. The barrier coefficient $\alpha \in (0, 1]$ controls the adjustment rate of barrier function \mathcal{B} during planning. Smaller α values impose stricter temporal constraints, promoting proactive collision avoidance. With $\alpha = 1$, the safety constraint reduces to the minimally restrictive form $\mathcal{B} \geq 0$, which is sufficient to guarantee recursive feasibility for arbitrary obstacle realizations according to Theorems 1–2. In practice, α effectively balances strict trajectory feasibility with proactive collision avoidance performance. Our experiments in Section V demonstrate that the proposed method still retains superior feasibility compared to alternative approaches even with $\alpha < 1$.

D. Contingency Planning with Consensus ADMM

1) *Reformulation of Trajectory Optimization:* Building upon the optimization problem (25), we present a compact and equivalent reformulation as follows:

$$\min_{\substack{\{c_\theta, c_x, c_y\} \\ \{\omega, d\}}} f(c_\theta) + f_x(c_x) + f_y(c_y) \quad (29a)$$

$$\text{s. t.} \quad F_0[c_x \ c_y] - [E_{x,0} \ E_{y,0}] = 0, \quad (29b)$$

$$F_{\theta,0}c_\theta = E_{\theta,0}, \quad F_{\theta,f}c_\theta = E_{\theta,f}, \quad (29c)$$

$$\omega \in \mathcal{C}_\omega, d \in \mathcal{C}_d, \quad (29d)$$

$$\mathcal{G}_{k,x} \triangleq \dot{\mathcal{B}}^T c_x - \mathbf{v} \cdot \cos \mathcal{B}^T c_\theta = 0, \quad (29e)$$

$$\mathcal{G}_{k,y} \triangleq \dot{\mathcal{B}}^T c_y - \mathbf{v} \cdot \sin \mathcal{B}^T c_\theta = 0, \quad (29f)$$

$$\mathcal{G}_{bo,x} \triangleq \mathcal{B}^T c_x^r - \mathcal{O}_x - l_x^r \cdot d^r \cdot \cos \omega^r = 0, \quad (29g)$$

$$\mathcal{G}_{bo,y} \triangleq \mathcal{B}^T c_y^r - \mathcal{O}_y - l_y^r \cdot d^r \cdot \sin \omega^r = 0, \quad (29h)$$

$$\mathcal{G}_{br,x} \triangleq \mathcal{B}^T c_x^s - \mathcal{R}_x - l_x^s \cdot d^s \cdot \cos \omega^s = 0, \quad (29i)$$

$$\mathcal{G}_{br,y} \triangleq \mathcal{B}^T c_y^s - \mathcal{R}_y - l_y^s \cdot d^s \cdot \sin \omega^s = 0, \quad (29j)$$

$$\mathcal{G}_{cs,x} \triangleq A_{c,x}^T c_x - Y_x = 0, \quad (29k)$$

$$\mathcal{G}_{cs,y} \triangleq A_{c,y}^T c_y - Y_y = 0, \quad (29l)$$

$$\mathcal{G}_{cs,\theta} \triangleq A_{c,\theta}^T c_\theta - Y_\theta = 0, \quad (29m)$$

$$\mathcal{G}_{c,x} \triangleq Gc_x - h_x \leq 0, \quad (29n)$$

$$\mathcal{G}_{c,y} \triangleq Gc_y - h_y \leq 0. \quad (29o)$$

Here, \triangleq denotes the definition operator for convenience. The optimization variables are denoted as $c_x = [c_x^r \ c_x^s] \in \mathbb{R}^{(n+1) \times 2}$, $c_\theta = [c_\theta^r \ c_\theta^s] \in \mathbb{R}^{(n+1) \times 2}$, and $c_y = [c_y^r \ c_y^s] \in \mathbb{R}^{(n+1) \times 2}$. The variables $\omega = [\omega^r \ \omega^s] \in \mathbb{R}^{(N \times M) \times 2}$ correspond to the matrix stacking relative angle ω_k^h , for M HVs within the planning horizon N , while $d = [d^r \ d^s] \in \mathbb{R}^{(N \times M) \times 2}$ follows an analogous structure. The cost function

(29a) comprises three components:

$$f(c_\theta) = \frac{1}{2} c_\theta^T Q_\theta c_\theta, \quad (30a)$$

$$f(c_x) = \frac{1}{2} c_x^T Q_x c_x + \frac{1}{2} \dot{c}_x^T \dot{B} Q_{x,v} \dot{B}^T c_x - v_{x,d}^T Q_{x,d} \dot{B}^T c_x, \quad (30b)$$

$$f(c_y) = \frac{1}{2} c_y^T Q_y c_y + \frac{1}{2} \dot{c}_y^T \dot{B} Q_{y,v} \dot{B}^T c_y - v_{y,d}^T Q_{y,d} \dot{B}^T c_y, \quad (30c)$$

where Q_θ , Q_x , Q_y , $Q_{x,v}$, $Q_{x,d}$, $Q_{y,v}$, and $Q_{y,d}$ denote symmetric positive semi-definite weighting matrices.

The constraint matrices for the initial and terminal state constraints (29b)-(29c) are given by $F_0 = [\mathcal{B}_0 \dot{\mathcal{B}}_0 \ddot{\mathcal{B}}_0]^T \in \mathbb{R}^{3 \times (n+1)}$, $F_{\theta,0} = [\mathcal{B}_0 \dot{\mathcal{B}}_0]^T \in \mathbb{R}^{2 \times (n+1)}$, and $F_{\theta,f} = [\mathcal{B}_N \dot{\mathcal{B}}_N]^T \in \mathbb{R}^{2 \times (n+1)}$, respectively. The vectors $E_{x,0}, E_{y,0} \in \mathbb{R}^{3 \times 2}$ encode the initial position, velocity and acceleration constraints along longitudinal and lateral components for both nominal and contingency trajectories, while $E_{\theta,0}, E_{\theta,f} \in \mathbb{R}^{2 \times 2}$ encode the initial and terminal state vectors for orientation angles and angular velocities.

The kinematic constraints (29e) and (29f) derived from (25e) and (25f), respectively, are enforced through the composite speed matrix $\mathbf{v} = [\mathbf{v}^r \ \mathbf{v}^s] \in \mathbb{R}^{N \times 2}$, where \mathbf{v}^r and \mathbf{v}^s represent the speed profiles for the nominal and contingency trajectories over the N -step horizon.

The collision avoidance constraints (29g)-(29h) and (29i)-(29j) correspond to the safety conditions (25i) and (25j), respectively. The predicted longitudinal and lateral positions of HVs for the nominal trajectory are denoted by $\mathcal{O}_x, \mathcal{O}_y \in \mathbb{R}^{N \times M}$ while $\mathcal{R}_x, \mathcal{R}_y \in \mathbb{R}^{N \times M}$ represent the corresponding FRS occupancy centers for the contingency trajectory. The safety ellipsoid dimension $l_x^r \in \mathbb{R}^{N \times M}$ is constructed by stacking l_x^h along the nominal trajectory, while l_y^r, l_x^s, l_y^s are constructed analogously.

For the state constraints (29n) and (29o) implementing (25c), the constraint matrix $G = [\mathcal{B}^T - \mathcal{B}^T \dot{\mathcal{B}}^T - \dot{\mathcal{B}}^T \ddot{\mathcal{B}}^T - \ddot{\mathcal{B}}^T]^T \in \mathbb{R}^{6N \times (n+1)}$ is constructed from $\mathcal{B} = [\mathcal{B}_1 \dots \mathcal{B}_N] \in \mathbb{R}^{(n+1) \times N}$. The matrices $h_x, h_y \in \mathbb{R}^{6N \times 2}$ contain the corresponding state bounds for longitudinal and lateral motions, respectively.

The constraints (29k)-(29m) enforce trajectory consistency for position, velocity, and acceleration at the initial segments between two trajectories. The corresponding matrices are $A_{c,x} = A_{c,y} = [\mathcal{B}_{[1:N_s]}^T \ \dot{\mathcal{B}}_{[1:N_s]}^T \ \ddot{\mathcal{B}}_{[1:N_s]}^T]^T \in \mathbb{R}^{((n+1) \times 3) \times N_s}$ and $A_{c,\theta} = \mathcal{B}_{[1:N_s]} \in \mathbb{R}^{(n+1) \times N_s}$. For the consensus variables, each column of $Y_x \in \mathbb{R}^{3N_s \times N_c}$, $Y_y \in \mathbb{R}^{3N_s \times N_c}$, and $Y_\theta \in \mathbb{R}^{N_s \times N_c}$ maintains consistency across candidate trajectories during ADMM iterations.

2) *ADMM Iterations*: The barrier constraints (29g)-(29j) exhibit biconvexity in $[c_x \ c_y \ d]^T$ and $[\cos \omega \ \sin \omega]^T$. This biconvex structure allows decomposition of the joint constraints (29g)-(29j) into two alternating optimizations: (i) Position optimization of $[c_x \ c_y]^T$ and d with fixed ω ; (ii) Angular optimization of ω with fixed $[c_x \ c_y]^T$ and d . Similarly, the kinematic constraints (29e)-(29f) admit an analogous decomposition, alternating between position variables $[c_x \ c_y]^T$ (fixed c_θ) and heading angle c_θ (fixed $[c_x \ c_y]^T$). Given that the quadratic objective (29a) preserves convexity, this constraint structure enables efficient ADMM-based decomposition of (29) into quadratic programming (QP) subproblems.

We derive an augmented Lagrangian of (29) for ADMM iterations, as follows:

$$\begin{aligned} \mathcal{L}(c_x, c_y, c_\theta, Z_x, Z_y, \omega, d, Y_x, Y_y, Y_\theta) \\ \lambda_x, \lambda_y, \lambda_\theta, \lambda_{\text{obs},x}, \lambda_{\text{obs},y}, \lambda_{c,x}, \lambda_{c,y}, \lambda_{c,\theta}) \\ = f_x(c_x) + f_y(c_y) + f(c_\theta) + \mathcal{I}_+(Z_x) + \mathcal{I}_+(Z_y) \\ + \lambda_x^T c_x + \lambda_y^T c_y + \rho_x \|\mathcal{G}_{c,x} + Z_x\|_2^2 + \rho_y \|\mathcal{G}_{c,y} + Z_y\|_2^2 \\ + \rho_\theta \left\| \mathcal{G}_{k,x} + \frac{\lambda_\theta}{\rho_\theta} \right\|_2^2 + \rho_\theta \left\| \mathcal{G}_{k,y} + \frac{\lambda_\theta}{\rho_\theta} \right\|_2^2 \\ + \rho_{\text{obs}}^r \left\| \mathcal{G}_{bo,x} + \frac{\lambda_{\text{obs},x}^r}{\rho_{\text{obs}}^r} \right\|_2^2 + \rho_{\text{obs}}^r \left\| \mathcal{G}_{bo,y} + \frac{\lambda_{\text{obs},y}^r}{\rho_{\text{obs}}^r} \right\|_2^2 \\ + \rho_{\text{obs}}^s \left\| \mathcal{G}_{br,x} + \frac{\lambda_{\text{obs},x}^s}{\rho_{\text{obs}}^s} \right\|_2^2 + \rho_{\text{obs}}^s \left\| \mathcal{G}_{br,y} + \frac{\lambda_{\text{obs},y}^s}{\rho_{\text{obs}}^s} \right\|_2^2 \\ + \rho_{c,x} \left\| \mathcal{G}_{cs,x} + \frac{\lambda_{c,x}}{\rho_{c,x}} \right\|_2^2 + \rho_{c,y} \left\| \mathcal{G}_{cs,y} + \frac{\lambda_{c,y}}{\rho_{c,y}} \right\|_2^2 \\ + \rho_{c,\theta} \left\| \mathcal{G}_{cs,\theta} + \frac{\lambda_{c,\theta}}{\rho_{c,\theta}} \right\|_2^2. \end{aligned} \quad (31)$$

In this formulation, the dual variables $\lambda_x, \lambda_y \in \mathbb{R}^{(n+1) \times 2}$ correspond to inequality constraints (29n)-(29o) for iteration stability, following [59]; $\rho_x, \rho_y, \rho_\theta, \rho_{\text{obs}}^r$, and ρ_{obs}^s denote the associated l_2 penalty parameters. The consensus dual variables $\lambda_{c,x} = [\lambda_{c,x}^r \ \lambda_{c,x}^s] \in \mathbb{R}^{3N_s \times 2}$, $\lambda_{c,y} = [\lambda_{c,y}^r \ \lambda_{c,y}^s] \in \mathbb{R}^{3N_s \times 2}$ and $\lambda_{c,\theta} = [\lambda_{c,\theta}^r \ \lambda_{c,\theta}^s] \in \mathbb{R}^{N_s \times 2}$ enforce the constraints (29k)-(29m); $\rho_{c,x}, \rho_{c,y}, \rho_{c,\theta}$ are the corresponding l_2 penalty parameters, driving local variables toward their consensus global values Y_x, Y_y , and Y_θ . The remaining dual variables $\lambda_\theta \in \mathbb{R}^{N \times 2}$, $\lambda_{\text{obs},x} = [\lambda_{\text{obs},x}^r \ \lambda_{\text{obs},x}^s] \in \mathbb{R}^{(N \times M) \times 2}$, and $\lambda_{\text{obs},y} = [\lambda_{\text{obs},y}^r \ \lambda_{\text{obs},y}^s] \in \mathbb{R}^{(N \times M) \times 2}$ are assigned to the constraints (29g)-(29j). We introduce slack variables Z_x, Z_y to handle potential constraint violations in (29n) and (29o). The indicator function $\mathcal{I}_+(\cdot)$ enforces exact constraint satisfaction: $\mathcal{I}_+(Z) = 0$ if $Z \geq 0$, and ∞ otherwise.

Following the ADMM framework [2], the augmented Lagrangian function (31) naturally partitions the primal variables into five distinct groups for alternate optimization: heading angle c_θ , longitudinal variables $\{c_x, Z_x\}$, lateral variables $\{c_y, Z_y\}$, angular variables ω , and distance variables d .

Primal Update. The primal variables are updated sequentially by solving the following QP subproblems:

$$c_\theta^{\iota+1} = \underset{c_\theta}{\operatorname{argmin}} \ \mathcal{L}(c_\theta, \{\cdot\}^\iota) \text{ s.t. } [F_{\theta,0} \ F_{\theta,f}] c_\theta = [E_{\theta,0} \ E_{\theta,f}],$$

$$c_x^{\iota+1} = \underset{c_x}{\operatorname{argmin}} \ \mathcal{L}(c_x, c_\theta^{\iota+1}, \{\cdot\}^\iota) \text{ s.t. } F_0 c_x = E_{x,0},$$

$$c_y^{\iota+1} = \underset{c_y}{\operatorname{argmin}} \ \mathcal{L}(c_y, c_x^{\iota+1}, c_\theta^{\iota+1}, \{\cdot\}^\iota) \text{ s.t. } F_0 c_y = E_{y,0},$$

where $\{\cdot\}^\iota$ compactly represents all other variables of \mathcal{L} fixed at iteration ι .

To handle the slack variables Z_x, Z_y for the inequality constraints (29n)-(29o), the iteration follows the form

$$Z_\bullet^{\iota+1} = \max(0, F_\bullet - G c_\bullet^{\iota+1}), \quad \bullet \in \{x, y\}$$

to strictly enforce the inequality constraints [60].

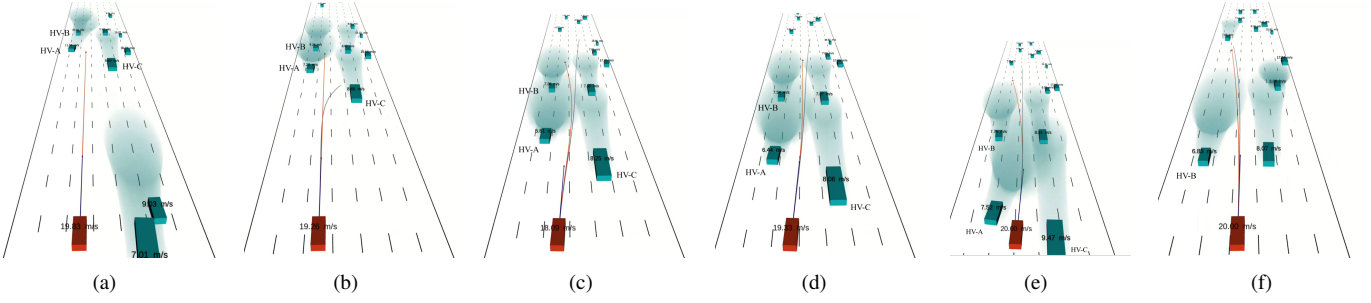


Fig. 3. Snapshots of the EV navigating dense traffic in the NGSIM dataset. The EV (red) jointly optimizes a nominal trajectory (red) and a contingency trajectory (black), with blue arrows showing velocities. The EV dynamically captures the uncertain intentions of HVs with online updating FRSs (shaded regions) and proactively responds to the potential cut-in of HV-A.

By leveraging the conditions in (22) and (23), we derive analytical solutions for ω and d :

$$\begin{aligned}\omega^{r,\ell+1} &= \arctan \left(\frac{l_x^r \cdot (\mathbf{v}^r c_y^{\ell+1} - \mathcal{O}_y)}{l_y^r \cdot (\mathbf{v}^r c_x^{\ell+1} - \mathcal{O}_x)} \right), \\ \omega^{s,\ell+1} &= \arctan \left(\frac{l_x^s \cdot (\mathbf{v}^s c_y^{\ell+1} - \mathcal{R}_y)}{l_y^s \cdot (\mathbf{v}^s c_x^{\ell+1} - \mathcal{R}_x)} \right), \\ d^{\ell+1} &= \max \left(1, 1 + (1 - \alpha)(d^\ell - 1) \right).\end{aligned}$$

Consensus Variables Update. As established in [61], the dual variables for consensus constraints maintain the zero-mean property:

$$\lambda_{c,\bullet}^{r,\ell} + \lambda_{c,\bullet}^{s,\ell} = 0, \quad \bullet \in \{x, y, \theta\}.$$

This structural property persists through ADMM iterations. The global variables update according to:

$$Y_{\bullet}^{\ell+1}[:, 0] = Y_{\bullet}^{\ell+1}[:, 1] = \frac{1}{2} A_{c,\bullet}^T \left(c_{\bullet}^{\ell+1}[:, 0] + c_{\bullet}^{\ell+1}[:, 1] \right), \quad \bullet \in \{x, y, \theta\}.$$

Dual Variables Update. The dual variables are updated through:

$$\begin{aligned}\lambda_{\theta}^{\ell+1} &= \lambda_{\theta}^{\ell} + \rho_{\theta} \left(\mathcal{B}^T c_{\theta}^{\ell+1} - \arctan \left(\frac{\dot{\mathcal{B}}^T c_y^{\ell+1}}{\dot{\mathcal{B}}^T c_x^{\ell+1}} \right) \right), \\ \lambda_{\bullet}^{\ell+1} &= \lambda_{\bullet}^{\ell} + \rho_{\bullet} \left((1 - \alpha_{\bullet})(Z_{\bullet}^{\ell+1} - Z_{\bullet}^{\ell}) \right. \\ &\quad \left. + \alpha_{\bullet}(G c_{\bullet}^{\ell+1} - F_{\bullet} + Z_{\bullet}^{\ell+1}) \right), \\ \lambda_{\text{obs},\bullet}^{r,\ell+1} &= \lambda_{\text{obs},\bullet}^{r,\ell} + \rho_{\text{obs}}^r \left(\mathbf{v}^r c_{\bullet}^{r,\ell+1} - \mathcal{O}_{\bullet} - l_{\bullet}^r d^{r,\ell+1} \cos(\omega^{r,\ell+1}) \right), \\ \lambda_{\text{obs},\bullet}^{s,\ell+1} &= \lambda_{\text{obs},\bullet}^{s,\ell} + \rho_{\text{obs}}^s \left(\mathbf{v}^s c_{\bullet}^{s,\ell+1} - \mathcal{R}_{\bullet} - l_{\bullet}^s d^{s,\ell+1} \cos(\omega^{s,\ell+1}) \right), \\ \lambda_{c,\theta}^{\ell+1} &= \lambda_{c,\theta}^{\ell} + \rho_{\theta} (A_{c,\theta}^T c_{\theta}^{\ell+1} - Y_{\theta}^{\ell+1}), \\ \lambda_{c,\bullet}^{\ell+1} &= \lambda_{c,\bullet}^{\ell} + \rho_{c,\bullet} (A_{c,\bullet}^T c_{\bullet}^{\ell+1} - Y_{\bullet}^{\ell+1}), \quad \bullet \in \{x, y\}.\end{aligned}$$

The iteration terminates when either the primal residual falls below $\epsilon^{\text{pri}} = 0.5$ or the maximum iteration count $\ell_{\max} = 200$ is reached, ensuring balanced computational efficiency and solution accuracy.

V. RESULTS

This section presents a comprehensive evaluation of the proposed approach through both high-fidelity simulations and real-world experiments. The simulation study constructs an urban intersection scenario and utilizes safety-critical highway

scenarios from the Next Generation Simulation (NGSIM) dataset¹, while physical validation is conducted using a 1:10-scale Ackermann-steering platform operating with HVs exhibiting diverse driving behaviors.

A. Simulation

1) Simulation Setup: The simulations are implemented in C++ running on an Ubuntu 24.04 LTS system with an Intel Ultra 9 285H CPU with 16 cores and 32 threads. The visualization uses RViz in ROS Noetic with a 100 Hz communication rate, while the planning loop operates with a time step $\delta T = 0.08$ s and a planning horizon $N = 50$ for both nominal and safe contingency trajectories.

The diagonal elements of the weighting matrices in (29a) are set to 50 for $Q_x, Q_y, Q_{\theta}, Q_{xv}, Q_{yv}$, and 100 for Q_{xd}, Q_{yd} . All L_2 penalty parameters in (31) are set to 5. The barrier coefficient parameter α is set to 0.8. The HV geometric ellipsoid axes l_x^h and l_y^h are set to 6 m and 4 m in the intersection scenario, and set according to their actual shapes in the highway dataset. The Bézier curve order n is set to 10. Acceleration bounds of ± 5 m/s² are enforced in both longitudinal and lateral directions. The terminal angular velocity of the orientation is set to zero. The considered HV number is set as $M = 4$. The consensus step N_s is set to 5. The control-intent set is initialized with ± 0.2 m/s² for longitudinal acceleration bounds and ± 0.1 m/s² for lateral acceleration bounds.

We evaluate five approaches:

- Proposed Safe Contingency Planner:** Our complete framework integrating online-updated FRS-based barrier constraints with contingency planning;
- Deterministic Barrier Planner:** A variant of our planner replacing the FRS-based barrier constraint (25j) with nominal barrier constraint (25i) in both nominal and contingency branches;
- Worst-Case Barrier Planner:** A conservative version using worst-case FRS predictions (derived from a prior control-intent set with ± 3 m/s² acceleration bounds) instead of online-updated FRS in (25j);
- ST-RHC [7]:** A baseline NMPC method using constant-velocity prediction for collision-avoidance constraints,

¹<https://data.transportation.gov/Automobiles/Next-Generation-Simulation-NGSIM-Vehicle-Trajectory/8ect-6jqq>

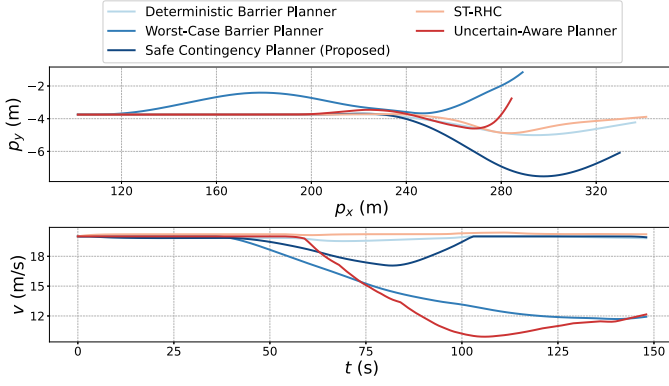


Fig. 4. Trajectory and speed profiles of the EV under different planning methods in the highway scenario. Our method proactively adjusts speed and starts lateral evasion early to defend HV-A's uncertain maneuvers without excessive conservatism.

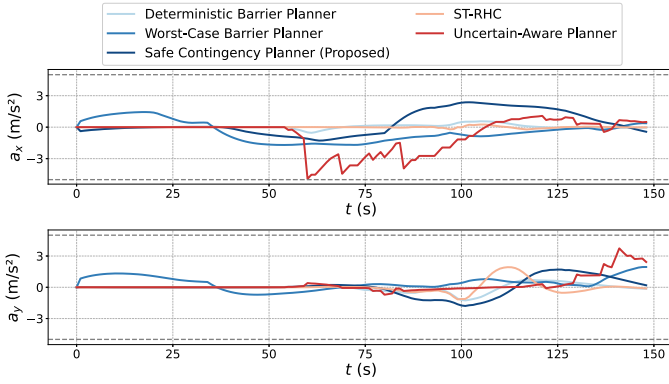


Fig. 5. Evolution of longitudinal and lateral acceleration profiles of EV with different planning methods (bounds shown as dashed lines). Our method shows proactive deceleration followed by smooth lateral avoidance during HV-A's abrupt cut-in maneuver.

solved efficiently through ACADO toolkit [62] with multiple shooting and sequential quadratic programming;

- (e) **Uncertain-Aware Planner** [44]: A baseline uncertain-aware planner embeds FRSs directly in NMPC solved with ACADO in C++, maintaining identical FRS update parameters for fair comparison.

The comprehensive evaluation incorporates four key performance metrics:

- **Safety Performance:** Collision rate P_c and the minimum distance to the nearest HV d_{\min} ;
- **Comfort:** Peak longitudinal/lateral jerk $J_{x,\max}$, $J_{y,\max}$;
- **Driving Efficiency:** Mean speed v_{mean} and travel distance s_{mean} ;
- **Computation:** Mean computation time t_{mean} .

1) Highway Cut-in Scenario on NGSIM.

The validation leverages challenging dense traffic driving scenarios from the NGSIM dataset to rigorously assess the performance. In the tested scenario, the EV navigates a multi-lane highway environment. As shown in Fig. 3, the HV-A in the leftmost lane initiates a rightward staged lane change, briefly pauses in the second leftmost lane, and then abruptly resumes its rightward maneuver just as the EV approaches.

TABLE I
PERFORMANCE EVALUATION ACROSS KEY METRICS

Method	Safety		Comfort		Efficiency		Time
	P_c (%)	d_{\min} (m)	$J_{x,\max}$ (m/s ³)	$J_{y,\max}$ (m/s ³)	v_{mean} (m/s)	s_{mean} (m)	t_{mean} (s)
Deter. Barr. Pl.	27.27	0.31	5.00	3.21	19.86	234.05	0.035
Wors. Barr. Pl.	0.00	6.53	6.17	7.08	15.75	186.07	0.033
Proposed	0.00	1.48	4.41	3.13	19.31	228.38	0.034
ST-RHC [7]	18.18	0.35	6.39	3.83	20.21	239.49	0.029
Uncert. Pl. [44]	0.00	5.61	9.67	10.23	14.28	168.16	0.038

Meanwhile, the HV-B and HV-C maintain steady driving. This scenario challenges the EV's ability to dynamically identify and adapt to uncertain HV intentions while proactively responding to potential cut-ins.

The simulation configuration establishes an initial EV speed of 20 m/s, with time headways to HV-A systematically varied from 4.5 s to 5.5 s in 0.1 s increments to ensure statistical reliability, with each parameter tested three times. Perception noise is modeled as a zero-mean Gaussian distribution [63]. The standard deviations are modeled as decreasing functions of the EV-HV distance. For the noise in longitudinal position, the standard deviation is $\sigma_{p_x}^h = \bar{\sigma}_{p_x} / \max\left(\frac{10}{s^h + 0.1}, 1\right)$, where s^h denotes the EV-HV distance and $\bar{\sigma}_{p_x} = 0.2$ m is a noise parameter. The same principle applies to the lateral position, longitudinal and lateral velocity components, with the corresponding noise parameters set as $\bar{\sigma}_{p_y} = 0.2$ m, $\bar{\sigma}_{v_x} = 0.1$ m/s and $\bar{\sigma}_{v_y} = 0.1$ m/s, respectively.

The performance evaluation presented in Table I demonstrates that the proposed method achieves collision-free with a safe minimum EV-HV distance of 1.48 m, while maintaining comfort requirements and competitive efficiency metrics. It represents significant improvements over both the Deterministic Barrier Planner with 27.27% collision rate and ST-RHC with 18.18% collision rate. This safety assurance stems from our rigorous FRS-based barrier constraints.

Trajectory analysis in Fig. 4 and Fig. 5 reveals distinct behavioral patterns among the compared methods. The proposed approach exhibits defensive characteristics through gradual deceleration initiated at approximately 40 s to anticipate potential cut-in maneuvers by HV-A. This proactive strategy enables smooth speed adjustment combined with moderate lateral avoidance when HV-A executes its sudden lane change, ensuring safe passage. In contrast, the Worst-Case Barrier method exhibits overly conservative behaviors, implementing premature, exaggerated deceleration and lateral displacement, substantially compromising driving efficiency. Meanwhile, the ST-RHC, relying exclusively on deterministic predictions, resorts to last-minute aggressive avoidance maneuvers when confronted with actual cut-in situations. Notably, our method demonstrates significant comfort improvements, reducing peak longitudinal and lateral jerk by 31.0% and 18.3% respectively compared to ST-RHC.

Moreover, comparative analysis with the Uncertain-Aware Planner [44] shows superior performance of our method in both driving efficiency and comfort. While this baseline approach directly employs FRS for obstacle avoidance, its lack

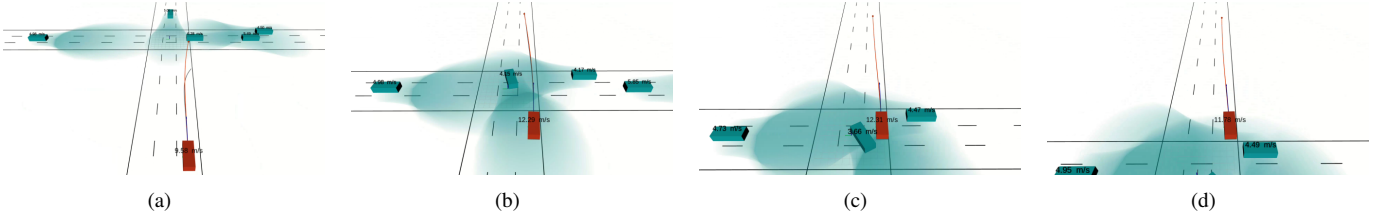


Fig. 6. Snapshots of the EV safely navigating through an unsignalized intersection. (a)-(d) demonstrate the EV's (red) response to a southbound HV's abrupt right turn while handling uncertainties from crossing traffic flows. Online updating HV FRSs are visualized as shaded regions.

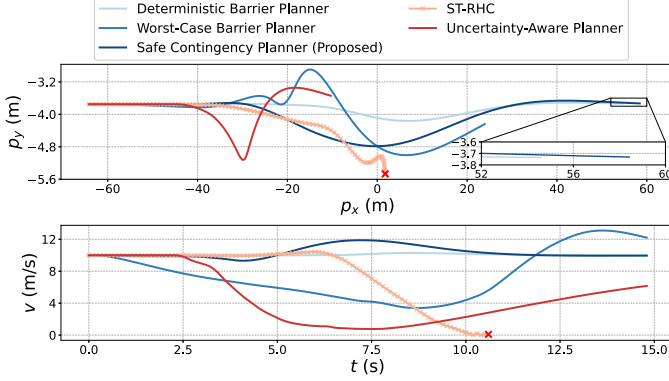


Fig. 7. Trajectory comparison in the intersection scenario demonstrates coordinated defensive deceleration and proactive lateral adjustments using the proposed method, achieving the longest navigation distance. While both the Deterministic Barrier Planner and ST-RHC result in collision (with ST-RHC additionally suffering from planner infeasibility, indicated by red crosses), the Worst-Case Barrier Planner and Uncertainty-Aware Planner exhibit excessive caution with unnecessary deceleration.

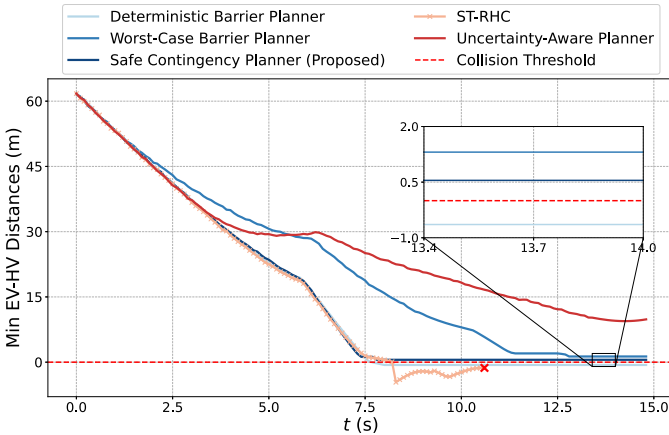


Fig. 8. The minimum EV-HV distances (d_{\min}) show that our method maintains appropriate safety margins. The Deterministic Barrier Planner and ST-RHC fail to avoid collision, while the Worst-case Barrier Planner and the Uncertainty-Aware planner exhibit unnecessarily conservative distances.

of contingency planning capability results in abrupt lateral maneuvers and degraded driving efficiency. The discontinuous nature of FRS updates leads to sudden trajectory adjustments, manifesting as high lateral jerk. Our method addresses these limitations through integrating FRS-based barrier constraint in contingency planning, achieving a 64.4% reduction in lateral jerk while maintaining smoother acceleration profiles within

constraints.

From a computational perspective, the proposed approach achieves real-time performance with 0.034 s per iteration. Biconvex structure exploitation with ADMM enables reliable real-time optimization for autonomous driving.

2) Urban Intersection Scenario. To further rigorously evaluate the capability of handling emergent traffic conflicts under uncertainty, we conduct a high-risk unsignalized intersection scenario test. The EV navigates northbound at 10 m/s through dense east-west traffic (6–10 m/s) along y axis. The critical challenge arises when an oncoming southbound HV along the x axis initially exhibits normal driving behavior before abruptly executing a right turn across the intended path of the EV. This scenario specifically tests two key capabilities: (1) proactive defensive maneuvers to account for trajectory prediction inaccuracies, and (2) simultaneous management of multi-vehicle motion uncertainties while ensuring safety.

The trajectory analysis in Figs. 6–7 shows safe navigation of our method through anticipatory deceleration and controlled rightward avoidance maneuvers, while maintaining minimum 0.55 m clearance from adjacent vehicles, as shown in Fig. 8. This defensive strategy achieves the longest travel distance (122.68 m) among all methods, optimally balancing safety and efficiency.

Comparative analysis reveals distinct limitations of baseline methods. The ST-RHC approach, relying on deterministic constant-velocity predictions, fails to anticipate the right-turning HV's maneuver, resulting in a collision due to rapidly shrinking feasible space between adjacent vehicles, ultimately leading to planner infeasibility. Parallel deficiencies emerge in the Deterministic Barrier Planner, which fails to adequately handle uncertain HV behaviors without FRS-based barrier constraints.

While the Worst-Case Barrier Planner ensures safety through excessive early deceleration and complete yielding, this approach severely compromises efficiency by requiring the EV to wait for complete intersection clearance. This result highlights the necessity of our online update mechanism for FRS predictions, adapting to observed behaviors rather than assuming worst-case behaviors. Similarly, the Uncertainty-Aware Planner with direct FRS constraint incorporation results in overly cautious behaviors with substantial speed reduction and the shortest travel distance. This limitation originates from directly embedding FRS constraints in the ST-RHC framework while lacking contingency optimization.

These findings collectively underscore the capability of our method to preserve safe contingency trajectories with feasibility in uncertain traffic conflicts.

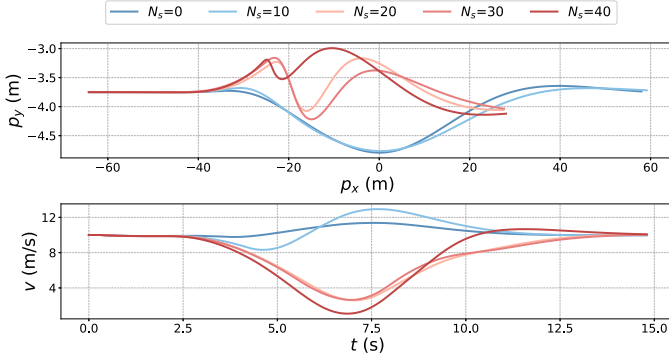


Fig. 9. Impact of the consensus step parameter N_s on intersection navigation behaviors. Smaller values enable aggressive maneuvers while larger values enforce conservative strategies with preemptive deceleration.

3) Discussion. The effectiveness of the proposed method is affected by two critical parameters: the consensus steps parameter N_s and the weight p_s . These parameters collectively determine how the vehicle balances immediate responsiveness with long-term performance in uncertain traffic scenarios.

N_s controls the consensus horizon shared by both trajectories. Fig. 9 shows smaller values ($N_s \leq 10$) enable more aggressive maneuvers by permitting earlier commitment to specific trajectory, with fixed $p_s = 0.5$. This can improve efficiency in most cases, but potentially reduce safety margins when HVs exhibit unexpected behaviors. Conversely, larger values ($N_s \geq 20$) enforce conservative behaviors by maintaining both deterministic and FRS-based constraints longer, often causing preemptive deceleration until intentions clarify. As demonstrated in Fig. 9, when N_s exceeds a certain threshold, the planner conservatively decelerates until the HV's intention becomes clear.

p_s regulates contingency branch weighting in optimization. Here we fix $N_s = 5$. As shown in Fig. 10, larger p_s values prioritize FRS-based safety barrier constraints in consensus segments, producing earlier and more pronounced deceleration. In contrast, smaller p_s values approximate deterministic planning that assumes perfect HV trajectory prediction, yielding reduced yet adequate safe margins.

For practical deployment, we recommend tailoring parameter configurations to specific operational requirements and desired conservatism levels. Although the method does not incorporate explicit risk quantification, it ensures safety when HV behaviors stay within the updated uncertainty bounds. Our analysis confirms that N_s and p_s effectively regulate the critical tradeoff between conservation and flexibility in uncertain traffic scenarios, allowing methodical adjustment of planning behavior across the safety-efficiency spectrum.

B. Experiment Results

To validate the practical efficacy of the proposed method, we conduct real-world experiments using 1:10-scale Ackermann-steering robotic platforms. The experimental setup consists of two robotic vehicles operating within an Optitrack motion capture system, with one serving as the EV and the other emulating the HV. The planning system, implemented

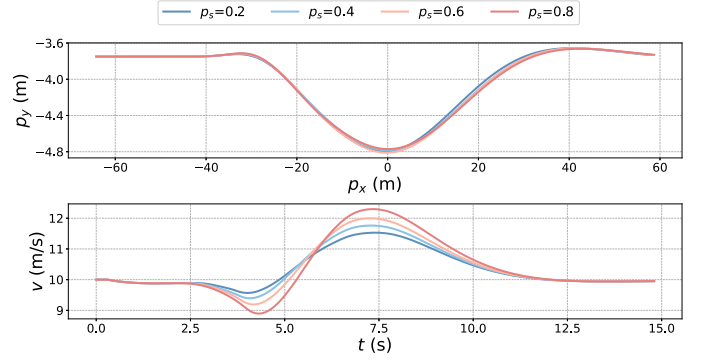


Fig. 10. Effect of the weighting parameter p_s on intersection navigation behaviors. Higher values emphasize FRS-based safety constraints, resulting in more defensive behaviors.

on a laptop with computational specifications matching our simulation platform, receives state feedback through ROS Noetic via wireless communication and generates appropriate control commands. Trajectory tracking is achieved through a linear feedback controller that demonstrates sufficient tracking accuracy for our experimental purposes.

We design safety-critical overtaking scenarios to rigorously evaluate the adaptive responsiveness to evolving environmental uncertainties. These scenarios specifically assess its ability to generate safe yet non-conservative trajectories while maintaining robustness against unpredictable lane intrusions. In the experimental configuration, the EV navigates along the reference path at $p_y = 0$ m with a desired speed of 3 m/s while attempting to overtake an HV moving from $p_y = -0.3$ m with varying degrees of aggressiveness. The experimental parameters are aligned with those used in the simulation.

Fig. 11 shows the snapshots in two experimental scenarios that highlight the algorithm performance under different HV uncertainties. In Scenario I, the HV exhibits aggressive, erratic behavior analogous to impaired driving, abruptly cutting into the EV's path at approximately $p_x = -2.8$ m. Scenario II presents the contrasting case where the HV maintains relatively steady lane intrusion behavior. These scenarios encapsulate the fundamental safety challenges addressed by our method, particularly the EV's need to continuously estimate potential hazardous maneuvers without prior knowledge, dynamically update the HV's reachable sets for real-time safety assurance, and maintain viable contingency plans against possible lane intrusions.

The planned and executed trajectories are depicted in Fig. 12. In Scenario I, the HV's erratic motions, caused by intentional hardware modifications to induce unpredictable behavior, creates significant uncertainty that prevents accurate trajectory prediction. Through online learning of the HV's control-intent set and subsequent FRS occupancy prediction, the EV successfully maintains both progress and safety. The resulting overtaking trajectory shows properly adaptive safety margin while effectively avoiding the HV's sudden lane intrusion towards $p_y = 0$ m. Scenario II confirms the inherent adaptability of the proposed approach, where the relatively steady HV behavior results in smaller predicted reachable sets, enabling the planner to naturally generate more efficient over-

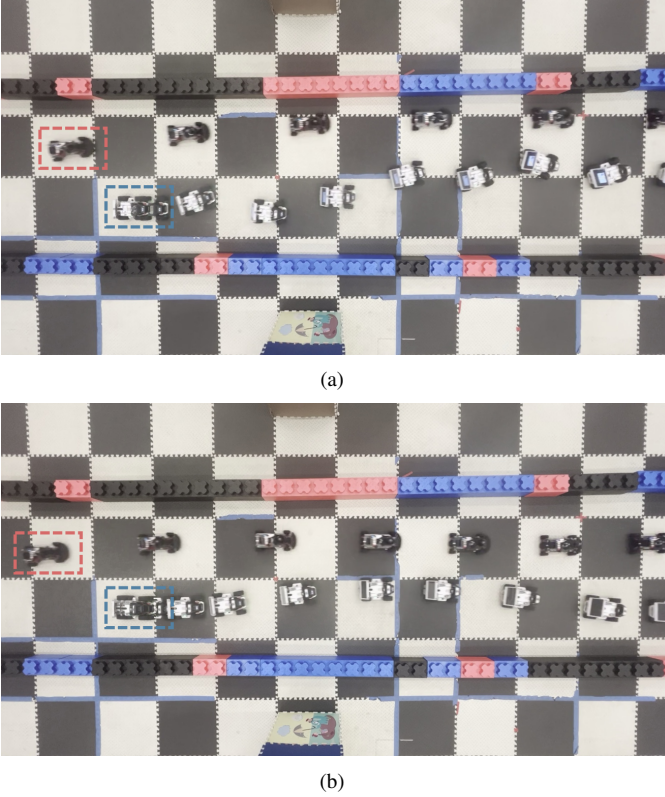


Fig. 11. Overlaying multiple frames of experiments showing (a) Scenario I: aggressive lane intrusion of HV, and (b) Scenario II: steady lane intrusion scenario of HV. The experiments highlight the adaptive safety assurance capabilities of the proposed method under varying HV uncertainties. The EV is outlined with a red dashed box, while the HV is marked with a blue dashed box.

taking trajectories with appropriately reduced conservatism.

Fig. 13 provides insight into the online adaptation mechanism governing the response to varying HV behaviors. The event $\|P_{u,m}^h u + q_{u,m}^h\|_2 \geq 1.0$ triggers the online learning of the control-intent sets given a newly collected control input vector u , leading to progressive expansion of set volume, computed by $\text{Vol}(\hat{\mathcal{U}}_m^h) = \pi \sqrt{\det(\Sigma_{u,m}^h)}$ [53]. Scenario I demonstrates rapid growth of set volume corresponding to the HV's aggressive maneuvers, while Scenario II maintains smaller sets with relatively steady behaviors. This adaptive learning mechanism inherent in the FRS-based safety barrier enables the planner to automatically adjust safety margins according to the perceived driving uncertainty, providing a principled approach to balancing safety and efficiency.

The physical experimental results demonstrate reliable and timely online update of varying FRS prediction through the event-triggered mechanism, which facilitates flexible adjustment of safety margins to match the perceived uncertain environment. Most importantly, the experimental outcomes verify that the planner generates non-conservative yet safe trajectories while maintaining defensive behaviors against sudden dangerous maneuvers, validating the practical applicability of our approach in safety-critical scenarios.

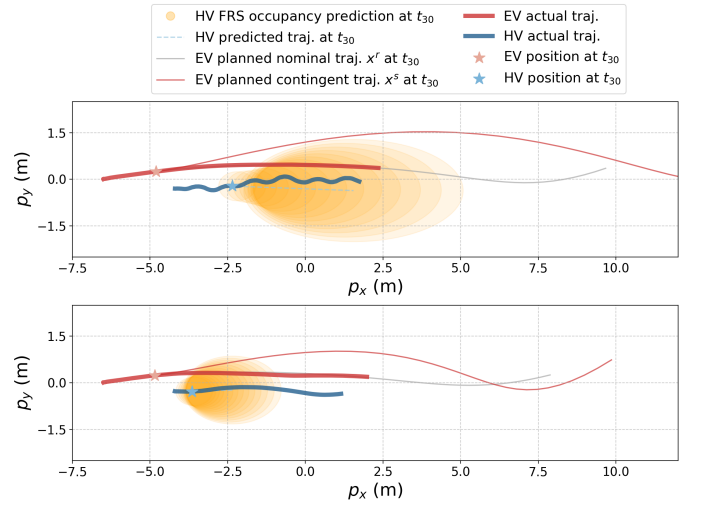


Fig. 12. Overtaking trajectory comparison under different uncertainty levels: (Top) Scenario I with erratic HV shows larger safety margins against intrusion risks; (Bottom) Scenario II with steady HV demonstrates relieved overtaking maneuvers with reduced conservatism. Shaded regions indicate FRS predictions, showing adaptability to varying uncertainty conditions.

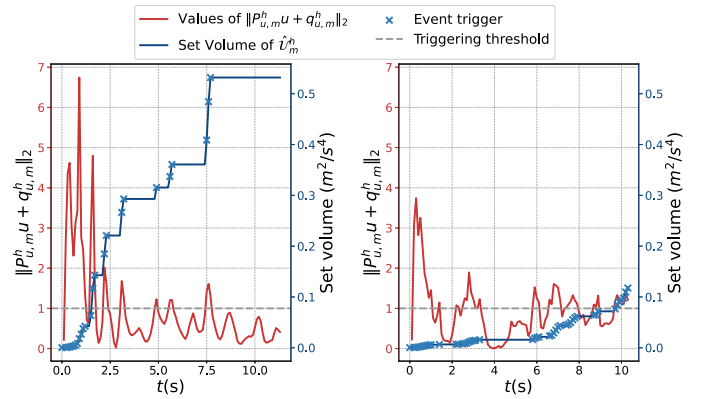


Fig. 13. Evolution of control-intent set volume during online learning. The triggering condition prompts updates of control-intent set $\hat{\mathcal{U}}_m^h$, with Scenario I (left) showing a more rapid increase of set volume corresponding to aggressive behaviors than that in Scenario II (right).

VI. CONCLUSIONS

In this study, we present a real-time trajectory optimization framework that generates safe and non-conservative trajectories through FRS-based barrier constraints with event-triggered online adaptive refinement. The method maintains feasible, safe trajectories under evolving uncertainties and avoids excessive conservatism or dangerous underestimation through incremental FRS updates. By decomposing the contingency optimization via consensus ADMM, the framework achieves computational efficiency for real-time implementation. Comprehensive validation demonstrates that the approach successfully achieves collision-free navigation with reduced jerks and maintains an average speed 14-20% higher than other baselines, preserving safety with balanced driving efficiency in dense traffic scenarios. Future research will extend this framework by incorporating game-theoretic interaction models, which would lead to more natural cooperative behaviors in dense traffic.

REFERENCES

- [1] L. Chen, Y. Li, C. Huang, B. Li, Y. Xing, D. Tian, L. Li, Z. Hu, X. Na, Z. Li *et al.*, “Milestones in autonomous driving and intelligent vehicles: Survey of surveys,” *IEEE Transactions on Intelligent Vehicles*, vol. 8, no. 2, pp. 1046–1056, 2022.
- [2] L. Zheng, R. Yang, M. Yu Wang, and J. Ma, “Barrier-enhanced parallel homotopic trajectory optimization for safety-critical autonomous driving,” *IEEE Transactions on Intelligent Transportation Systems*, vol. 26, no. 2, pp. 2169–2186, 2025.
- [3] T. Benciolini, C. Tang, M. Leibold, C. Weaver, M. Tomizuka, and W. Zhan, “Active exploration in iterative Gaussian process regression for uncertainty modeling in autonomous racing,” *IEEE Transactions on Control Systems Technology*, vol. 33, no. 4, pp. 1301–1316, 2025.
- [4] K. A. Mustafa, D. J. Ornia, J. Kober, and J. Alonso-Mora, “RACP: Risk-aware contingency planning with multi-modal predictions,” *IEEE Transactions on Intelligent Vehicles*, pp. 1–16, 2024.
- [5] L. Zhang, S. Han, and S. Grammatico, “Automated lane merging via game theory and branch model predictive control,” *IEEE Transactions on Control Systems Technology*, vol. 33, no. 4, pp. 1258–1269, 2025.
- [6] X. Zhang, S. Zeinali, and G. Schildbach, “Interaction-aware traffic prediction and scenario-based model predictive control for autonomous vehicles on highways,” *IEEE Transactions on Control Systems Technology*, vol. 33, no. 4, pp. 1235–1245, 2025.
- [7] L. Zheng, R. Yang, Z. Peng, M. Y. Wang, and J. Ma, “Spatiotemporal receding horizon control with proactive interaction towards autonomous driving in dense traffic,” *IEEE Transactions on Intelligent Vehicles*, vol. 9, no. 11, pp. 6853–6868, 2024.
- [8] M. Althoff and S. Magdici, “Set-based prediction of traffic participants on arbitrary road networks,” *IEEE Transactions on Intelligent Vehicles*, vol. 1, no. 2, pp. 187–202, 2016.
- [9] L. Gharavi, A. Dabiri, J. Verkuiljen, B. De Schutter, and S. Baldi, “Proactive emergency collision avoidance for automated driving in highway scenarios,” *IEEE Transactions on Control Systems Technology*, vol. 33, no. 4, pp. 1164–1177, 2025.
- [10] S. Ge and C.-H. Fua, “Queues and artificial potential trenches for multirobot formations,” *IEEE Transactions on Robotics*, vol. 21, no. 4, pp. 646–656, 2005.
- [11] H. Zhu and J. Alonso-Mora, “Chance-constrained collision avoidance for mavs in dynamic environments,” *IEEE Robotics and Automation Letters*, vol. 4, no. 2, pp. 776–783, 2019.
- [12] S. H. Nair, H. Lee, E. Joa, Y. Wang, H. E. Tseng, and F. Borrelli, “Predictive control for autonomous driving with uncertain, multimodal predictions,” *IEEE Transactions on Control Systems Technology*, vol. 33, no. 4, pp. 1178–1192, 2025.
- [13] O. de Groot, L. Ferranti, D. M. Gavrila, and J. Alonso-Mora, “Scenario-based motion planning with bounded probability of collision,” *The International Journal of Robotics Research*, 2025.
- [14] T. Brüdigam, M. Olbrich, D. Wollherr, and M. Leibold, “Stochastic model predictive control with a safety guarantee for automated driving,” *IEEE Transactions on Intelligent Vehicles*, vol. 8, no. 1, pp. 22–36, 2021.
- [15] K. Ren, C. Chen, H. Sung, H. Ahn, I. M. Mitchell, and M. Kamgarpour, “Recursively feasible chance-constrained model predictive control under gaussian mixture model uncertainty,” *IEEE Transactions on Control Systems Technology*, vol. 33, no. 4, pp. 1193–1206, 2025.
- [16] A. Wang, A. Jasour, and B. C. Williams, “Non-gaussian chance-constrained trajectory planning for autonomous vehicles under agent uncertainty,” *IEEE Robotics and Automation Letters*, vol. 5, no. 4, pp. 6041–6048, 2020.
- [17] O. de Groot, B. Brito, L. Ferranti, D. Gavrila, and J. Alonso-Mora, “Scenario-based trajectory optimization in uncertain dynamic environments,” *IEEE Robotics and Automation Letters*, vol. 6, no. 3, pp. 5389–5396, 2021.
- [18] A. Ben-Tal and A. Nemirovski, “Robust convex optimization,” *Mathematics of Operations Research*, vol. 23, no. 4, pp. 769–805, 1998.
- [19] Á. Carrizosa-Rendón, V. Puig, and F. Nejari, “Safe motion planner for autonomous driving based on LPV MPC and reachability analysis,” *Control Engineering Practice*, vol. 147, p. 105932, 2024.
- [20] H. Seo, D. Lee, C. Y. Son, I. Jang, C. J. Tomlin, and H. J. Kim, “Real-time robust receding horizon planning using Hamilton–Jacobi reachability analysis,” *IEEE Transactions on Robotics*, vol. 39, no. 1, pp. 90–109, 2022.
- [21] S. Manzingier, C. Pek, and M. Althoff, “Using reachable sets for trajectory planning of automated vehicles,” *IEEE Transactions on Intelligent Vehicles*, vol. 6, no. 2, pp. 232–248, 2020.
- [22] M. Koschi and M. Althoff, “Set-based prediction of traffic participants considering occlusions and traffic rules,” *IEEE Transactions on Intelligent Vehicles*, vol. 6, no. 2, pp. 249–265, 2020.
- [23] I. Batkovic, A. Gupta, M. Zanon, and P. Falcone, “Experimental validation of safe MPC for autonomous driving in uncertain environments,” *IEEE Transactions on Control Systems Technology*, vol. 31, no. 5, pp. 2027–2042, 2023.
- [24] T. Skibik, A. P. Vinod, A. Weiss, and S. Di Cairano, “MPC with integrated evasive maneuvers for failure-safe automated driving,” in *2023 American Control Conference (ACC)*, 2023, pp. 1122–1128.
- [25] C. Pek and M. Althoff, “Computationally efficient fail-safe trajectory planning for self-driving vehicles using convex optimization,” in *International Conference on Intelligent Transportation Systems (ITSC)*, 2018, pp. 1447–1454.
- [26] —, “Fail-safe motion planning for online verification of autonomous vehicles using convex optimization,” *IEEE Transactions on Robotics*, vol. 37, no. 3, pp. 798–814, 2020.
- [27] T. Benciolini, M. Fink, N. Güzelkaya, D. Wollherr, and M. Leibold, “Safe and non-conservative trajectory planning for autonomous driving handling unanticipated behaviors of traffic participants,” *arXiv preprint arXiv:2406.13396*, 2024.
- [28] S. Ejaz and M. Inoue, “Trust-aware safe control for autonomous navigation: Estimation of system-to-human trust for trust-adaptive control barrier functions,” *IEEE Transactions on Control Systems Technology*, vol. 33, no. 4, pp. 1151–1163, 2025.
- [29] X. Fang and W.-H. Chen, “Model predictive control with preview: Recursive feasibility and stability,” *IEEE Control Systems Letters*, vol. 6, pp. 2647–2652, 2022.
- [30] E. Kerrigan and J. Maciejowski, “Invariant sets for constrained nonlinear discrete-time systems with application to feasibility in model predictive control,” in *IEEE Conference on Decision and Control (CDC)*, vol. 5, 2000, pp. 4951–4956.
- [31] J. Zeng, B. Zhang, and K. Sreenath, “Safety-critical model predictive control with discrete-time control barrier function,” in *American Control Conference (ACC)*, 2021, pp. 3882–3889.
- [32] J. J. Choi, D. Lee, K. Sreenath, C. J. Tomlin, and S. L. Herbert, “Robust control barrier–value functions for safety-critical control,” in *IEEE Conference on Decision and Control (CDC)*, 2021, pp. 6814–6821.
- [33] A. R. Kumar, K.-C. Hsu, P. J. Ramadge, and J. F. Fisac, “Fast, smooth, and safe: implicit control barrier functions through reach-avoid differential dynamic programming,” *IEEE Control Systems Letters*, vol. 7, pp. 2994–2999, 2023.
- [34] J. Kim, J. Lee, and A. D. Ames, “Safety-critical coordination of legged robots via layered controllers and forward reachable set based control barrier functions,” in *IEEE International Conference on Robotics and Automation (ICRA)*, 2024, pp. 3478–3484.
- [35] Y. Gao, F. J. Jiang, L. Xie, and K. H. Johansson, “Risk-aware optimal control for automated overtaking with safety guarantees,” *IEEE Transactions on Control Systems Technology*, vol. 30, no. 4, pp. 1460–1472, 2021.
- [36] X. Wang, Z. Li, J. Alonso-Mora, and M. Wang, “Reachability-based confidence-aware probabilistic collision detection in highway driving,” *Engineering*, vol. 33, pp. 90–107, 2024.
- [37] S. Bansal, A. Bajcsy, E. Ratner, A. D. Dragan, and C. J. Tomlin, “A Hamilton–Jacobi reachability-based framework for predicting and analyzing human motion for safe planning,” in *IEEE International Conference on Robotics and Automation (ICRA)*, 2020, pp. 7149–7155.
- [38] K. Driggs-Campbell, R. Dong, and R. Bajcsy, “Robust, informative human-in-the-loop predictions via empirical reachable sets,” *IEEE Transactions on Intelligent Vehicles*, vol. 3, no. 3, pp. 300–309, 2018.
- [39] J. Xiang and J. Chen, “Convex approximation of probabilistic reachable sets from small samples using self-supervised neural networks,” *arXiv preprint arXiv:2411.14356*, 2024.
- [40] M. E. Cao, M. Bloch, and S. Coogan, “Estimating high probability reachable sets using Gaussian processes,” in *IEEE Conference on Decision and Control (CDC)*, 2021, pp. 3881–3886.
- [41] A. Devonport and M. Arcak, “Data-driven reachable set computation using adaptive gaussian process classification and monte carlo methods,” in *American control conference (ACC)*, 2020, pp. 2629–2634.
- [42] A. Chakrabarty, C. Danielson, S. Di Cairano, and A. Raghunathan, “Active learning for estimating reachable sets for systems with unknown dynamics,” *IEEE Transactions on Cybernetics*, vol. 52, no. 4, pp. 2531–2542, 2020.
- [43] J. Zhou, Y. Gao, O. Johansson, B. Olofsson, and E. Frisk, “Robust predictive motion planning by learning obstacle uncertainty,” *IEEE*

- Transactions on Control Systems Technology*, vol. 33, no. 3, pp. 1006–1020, 2025.
- [44] J. Zhou, Y. Gao, B. Olofsson, and E. Frisk, “Robust motion planning for autonomous vehicles based on environment and uncertainty-aware reachability prediction,” *Control Engineering Practice*, vol. 160, p. 106319, 2025.
 - [45] J. Hardy and M. Campbell, “Contingency planning over probabilistic obstacle predictions for autonomous road vehicles,” *IEEE Transactions on Robotics*, vol. 29, no. 4, pp. 913–929, 2013.
 - [46] Y. Chen, U. Rosolia, W. Ubellacker, N. Csomay-Shanklin, and A. D. Ames, “Interactive multi-modal motion planning with branch model predictive control,” *IEEE Robotics and Automation Letters*, vol. 7, no. 2, pp. 5365–5372, 2022.
 - [47] W. Zhan, C. Liu, C.-Y. Chan, and M. Tomizuka, “A non-conservatively defensive strategy for urban autonomous driving,” in *IEEE International Conference on Intelligent Transportation Systems (ITSC)*, 2016, pp. 459–464.
 - [48] X. Chen and J. Mårtensson, “Invariant safe contingency model predictive control for intersection coordination of mixed traffic,” in *IEEE International Conference on Intelligent Transportation Systems (ITSC)*, 2023, pp. 3369–3376.
 - [49] J. Ma, Z. Cheng, X. Zhang, M. Tomizuka, and T. H. Lee, “Alternating direction method of multipliers for constrained iterative LQR in autonomous driving,” *IEEE Transactions on Intelligent Transportation Systems*, vol. 23, no. 12, pp. 23 031–23 042, 2022.
 - [50] V. K. Adajania, A. Sharma, A. Gupta, H. Masnavi, K. M. Krishna, and A. K. Singh, “Multi-modal model predictive control through batch non-holonomic trajectory optimization: Application to highway driving,” *IEEE Robotics and Automation Letters*, vol. 7, no. 2, pp. 4220–4227, 2022.
 - [51] L. Zheng, R. Yang, M. Zheng, Z. Peng, M. Y. Wang, and J. Ma, “Occlusion-aware contingency safety-critical planning for autonomous vehicles,” *arXiv preprint arXiv:2502.06359*, 2025.
 - [52] Y. Chen, S. Veer, P. Karkus, and M. Pavone, “Interactive joint planning for autonomous vehicles,” *IEEE Robotics and Automation Letters*, vol. 9, no. 2, pp. 987–994, 2023.
 - [53] S. P. Boyd and L. Vandenberghe, *Convex Optimization*. Cambridge, UK: Cambridge University Press, 2004.
 - [54] M. J. Todd and E. A. Yildirim, “On Khachiyan’s algorithm for the computation of minimum-volume enclosing ellipsoids,” *Discrete Applied Mathematics*, vol. 155, no. 13, pp. 1731–1744, 2007.
 - [55] F. Berkenkamp, M. Turchetta, A. Schoellig, and A. Krause, “Safe model-based reinforcement learning with stability guarantees,” *Advances in Neural Information Processing Systems*, vol. 30, 2017.
 - [56] A. Agrawal and K. Sreenath, “Discrete control barrier functions for safety-critical control of discrete systems with application to bipedal robot navigation,” in *Robotics: Science and Systems*, 2017.
 - [57] G. Farin, *Curves and Surfaces for CAGD: A Practical Guide*, 5th ed. San Francisco, CA, USA: Morgan Kaufmann Publishers Inc., 2001.
 - [58] Y. Huang, J. Du, Z. Yang, Z. Zhou, L. Zhang, and H. Chen, “A survey on trajectory-prediction methods for autonomous driving,” *IEEE Transactions on Intelligent Vehicles*, vol. 7, no. 3, pp. 652–674, 2022.
 - [59] G. Taylor, R. Burmeister, Z. Xu, B. Singh, A. Patel, and T. Goldstein, “Training neural networks without gradients: A scalable ADMM approach,” in *International Conference on Machine Learning*, 2016, pp. 2722–2731.
 - [60] E. Ghadimi, A. Teixeira, I. Shames, and M. Johansson, “Optimal parameter selection for the alternating direction method of multipliers (ADMM): Quadratic problems,” *IEEE Transactions on Automatic Control*, vol. 60, no. 3, pp. 644–658, 2015.
 - [61] S. Boyd, N. Parikh, E. Chu, B. Peleato, J. Eckstein *et al.*, “Distributed optimization and statistical learning via the alternating direction method of multipliers,” *Foundations and Trends in Machine Learning*, vol. 3, no. 1, pp. 1–122, 2011.
 - [62] B. Houska, H. Ferreau, and M. Diehl, “ACADO toolkit – An open source framework for automatic control and dynamic optimization,” *Optimal Control Applications and Methods*, vol. 32, no. 3, pp. 298–312, 2011.
 - [63] L. Zheng, R. Yang, M. Zheng, M. Y. Wang, and J. Ma, “Safe and real-time consistent planning for autonomous vehicles in partially observed environments via parallel consensus optimization,” *IEEE Transactions on Intelligent Transportation Systems*, 2025.